Chapter 22
Micro/Nanotribology and Micro/Nanomechanics of Magnetic Storage Devices

Bharat Bhushan

Abstract A magnetic recording process involves relative motion between a magnetic medium (tape or disk) against a stationary or rotating read/write magnetic head. For ever-increasing, high areal recording density, the linear flux density (number of flux reversals per unit distance) and the track density (number of tracks per unit distance) should be as high as possible. The size of a single bit dimension for current devices is typically less than 1,000 nm^2. This dimension places stringent restrictions on the defect size present on the head and medium surfaces.

Reproduced (read-back) magnetic signal amplitude decreases with a decrease in the recording wavelength and/or the track width. The signal loss results from the magnetic coating thickness, read gap length, and head-to-medium spacing (clearance or flying height). It is known that the signal loss as a result of spacing can be reduced exponentially by reducing the separation between the head and the medium. The need for increasingly higher recording densities requires that surfaces be as smooth as possible and the flying height (physical separation or clearance between a head and a medium) be as low as possible. The ultimate objective is to run two surfaces in contact (with practically zero physical separation) if the tribological issues can be resolved. Smooth surfaces in near contact lead to an increase in adhesion, friction, and interface temperatures, and closer flying heights lead to occasional rubbing of high asperities and increased wear. Friction and wear issues are resolved by appropriate selection of interface materials and lubricants, by controlling the dynamics of the head and medium, and the environment. A fundamental understanding of the tribology (friction, wear, and lubrication) of the magnetic head/medium interface, both on macro- and micro/nanoscales, becomes crucial for the continued growth of this more than $ 60 billion a year magnetic storage industry.

In this chapter, initially, the general operation of drives and the construction and materials used in magnetic head and medium components are described. Then the micro/nanotribological and micro/nanomechanics studies including surface

B. Bhushan (ed.), *Nanotribology and Nanomechanics*,
DOI 10.1007/978-3-642-15263-4_22,

roughness, friction, adhesion, scratching, wear, indentation, and lubrication relevant to magnetic storage devices are presented.

22.1 Introduction

22.1.1 Magnetic Storage Devices

Magnetic storage devices used for storage and retrieval are tape, flexible (floppy) disk and rigid disk drives. These devices are used for audio, video and data-storage applications. Magnetic storage industry is some $ 60 billion a year industry with $ 20 billion for audio and video recording (almost all tape drives/media) and $ 40 billion for data storage. In the data-storage industry, magnetic rigid disk drives/media, tape drives/media, flexible disk drives/media, and optical disk drive/media account for about $ 25 B, $ 6 B, $ 3 B, and $ 6 B, respectively. Magnetic recording and playback involves the relative motion between a magnetic medium (tape or disk) against a read-write magnetic head. Heads are designed so that they develop a (load-carrying) hydrodynamic air film under steady operating conditions to minimize head-medium contact. However, physical contact between the medium and head occurs during starts and stops, referred to as contact-start-stops (CSS) technology [1–4]. In the modern magnetic storage devices, the flying heights (head-to-medium separation) are on the order of 5–20 nm and roughnesses of head and medium surfaces are on the order of 1–2 nm RMS. The need for ever-increasing recording densities requires that surfaces be as smooth as possible and the flying heights be as low as possible. Smooth surfaces lead to an increase in adhesion, friction, and interface temperatures, and closer flying heights lead to occasional rubbing of high asperities and increased wear. High stiction (static friction) and wear are the limiting technology to future of this industry. Head load/unload (L/UL) technology has recently been used as an alternative to CSS technology in rigid disk drives that eliminates stiction and wear failure mode associated with CSS. In an L/UL drive, a lift tab extending from the suspension load beam engages a ramp or cam structure as the actuator moves beyond the outer radius of the disk. The ramp lifts (or unloads) the head stack from the disk surfaces as the actuator moves to the parking position. Starting and stopping the disk only occur with the head in the unloaded state. Several contact or near contact recording devices are at various stages of development. High stiction and wear are the major impediments to the commercialization of the contact recording [1–7].

Magnetic media fall into two categories: particulate media, where magnetic particles (γ-Fe_2O_3, Co–γFe_2O_3, CrO_2, Fe or metal (MP), or barium ferrite) are dispersed in a polymeric matrix and coated onto a polymeric substrate for flexible media (tape and flexible disks); thin-film media, where continuous films of magnetic materials are deposited by vacuum deposition techniques onto a polymer substrate for flexible media or onto a rigid substrate (typically aluminium and more recently glass or glass ceramic) for rigid disks. The most commonly used thin

magnetic films for tapes are evaporated Co–Ni (82–18 at.%) or Co–O dual layer. Typical magnetic films for rigid disks are metal films of cobalt-based alloys (such as sputtered Co–Pt–Ni, Co–Ni, Co–Pt–Cr, Co–Cr and Co–NiCr). For high recording densities, trends have been to use thin-film media. Magnetic heads used to date are either conventional thin-film inductive, magnetoresistive (MR) and giant MR (GMR) heads. The air-bearing surfaces (ABS) of tape heads are generally cylindrical in shape. For dual-sided flexible-disk heads, two heads are either spherically contoured and slightly offset (to reduce normal pressure) or are flat and loaded against each other. The rigid-disk heads are supported by a leaf spring (flexure) suspension. The ABS of heads are almost made of Mn–Zn ferrite, Ni–Zn ferrite, Al_2O_3–TiC and calcium titanate. The ABS of some conventional heads are made of plasma sprayed coatings of hard materials such as Al_2O_3–TiO_2 and ZrO_2 [2–4].

Figure 22.1 shows the schematic illustrating the tape path with details of tape guides in a data-processing linear tape drive (IBM LTO Gen1) which uses a rectangular tape cartridge. Figure 22.2a shows the sectional views of particulate and thin-film magnetic tapes. Almost exclusively, the base film is made of semicrystalline biaxially-oriented poly (ethylene terephthalate) (or PET) or poly (ethylene 2,6 naphthalate) (or PEN) or Aramid. The particulate coating formulation consists of binder (typically polyester polyurethane), submicron accicular shaped magnetic particles (about 50 nm long with an aspect ratio of about 5), submicron head cleaning agents (typically alumina) and lubricant (typically fatty acid ester). For protection against wear and corrosion and low friction/stiction, the thin-film tape is first coated with a diamondlike carbon (DLC) overcoat deposited by plasma enhanced chemical vapor deposition, topically lubricated with primarily a perfluoropolyether lubricant. Figure 22.2b shows the schematic of an 8-track (along with 2 servo tracks) thin-film read-write head with MR read and inductive write. The head steps up and down to provide 384 total data tracks across the width of the tape. The ABS is made of Al_2O_3–TiC. A tape tension of about 1 N over a 12.7 mm wide tape (normal pressure $\approx$ 14 kPa) is used during use. The RMS roughnesses of ABS of the heads and tape surfaces typically are 1–1.5 nm and 5–8 nm, respectively.

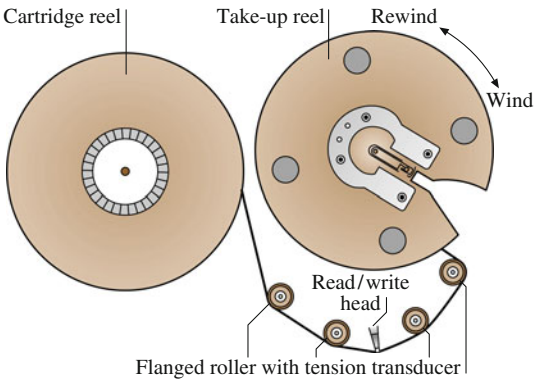

Fig. 22.1 Schematic of tape path in an IBM Linear Tape Open (LTO) tape drive

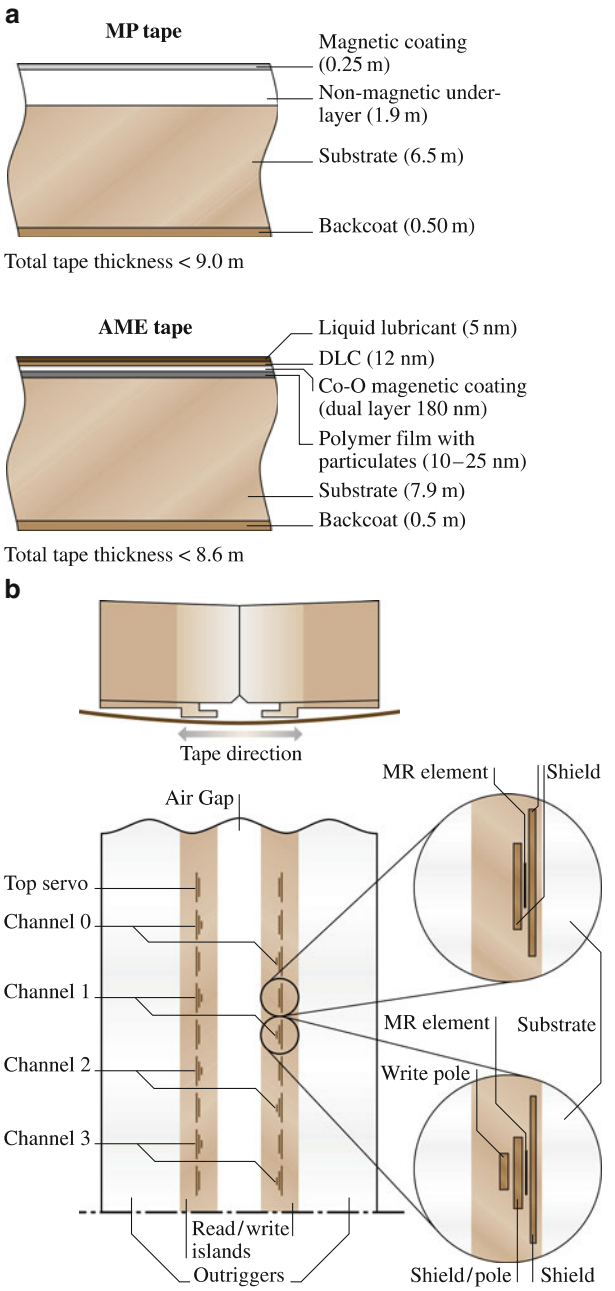

Fig. 22.2 (**a**) Sectional views of particulate and thin-film magnetic tapes, and (**b**) schematic of a magnetic thin-film read/write head for an IBM LTO Gen 1 tape drive

Figure 22.3 shows the schematic of a data processing rigid disk drive with 22.6-, 27.4-, 48-, 63.5-, 75-, and 95-mm form factor. Nonremovable stack of multiple disks mounted on a ball bearing or hydrodynamic spindle, are rotated by an electric motor at constant angular speed ranging from about 5,000 to in excess of 15,000 RPM, dependent upon the disk size. Head slider-suspension assembly (allowing one slider for each disk surface) is actuated by a stepper motor or a voice coil motor using a rotary actuator. Figure 22.4a shows the sectional views of a thin-film rigid disk. The substrate for rigid disks is generally a non heat-treatable aluminium–magnesium alloy 5086, glass or glass ceramic. The protective overcoat commonly used for thin-film disks is sputtered DLC, topically lubricated with perfluoropolyether

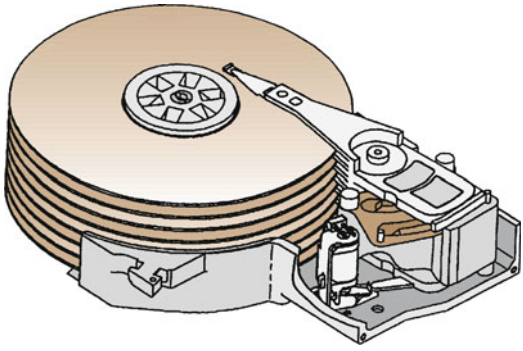

Fig. 22.3 Schematic of a data-processing magnetic rigid disk drive

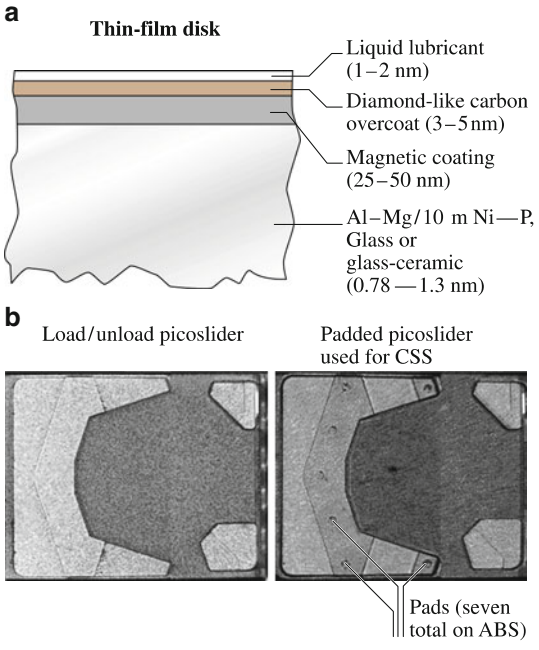

Fig. 22.4 (**a**) Sectional views of a thin-film magnetic rigid disk, and (**b**) schematic of two picosliders – load/unload picoslider and padded picoslider used for CSS

type of lubricants. Lubricants with polar-end groups are generally used for thin-film disks in order to provide partial chemical bonding to the overcoat surface. The disks used for CSS technology are laser textured in the landing zone. Figure 22.4b shows the schematic of two thin-film head picosliders with a step at the leading edge, and GMR read and inductive write. "Pico" refers to the small sizes of 1.25 mm × 1 mm. These sliders use Al_2O_3–TiC (70 − 30 wt%) as the substrate material with multilayered thin-film head structure coated and with about 3.5 nm thick DLC coating to prevent the thin film structure from electrostatic discharge. The seven pads on the padded slider are made of DLC and are about 40 μm in diameter and 50 nm in height. A normal load of about 3 g is applied during use.

22.1.2 Micro/Nanotribology and Micro/Nanomechanics and Their Applications

The micro/nanotribological studies are needed to develop fundamental understanding of interfacial phenomena on a small scale and to study interfacial phenomena in [8–12]. Magnetic storage devices operate under low load and encounter isolated asperity interactions. These use multilayered thin film structure and are generally lubricated with molecularly-thin films. Micro/nanotribological and micro/nanomechanical techniques are ideal to study the friction and wear processes of micro/nanoscale and molecularly thick films. These studies are also valuable in fundamental understanding of interfacial phenomena in macrostructures to provide a bridge between science and engineering. At interfaces of technological applications, contact occurs at multiple asperity contacts. A sharp tip of tip-based microscopes (atomic force/friction force microscopes or AFM/FFM) sliding on a surface simulates a single asperity contact, thus allowing high-resolution measurements of surface interactions at a single asperity contacts. AFMs/FFMs are now commonly used for tribological studies.

In this chapter, we present state-of-the-art of micro/nanotribology and micro/nanomechanics of magnetic storage devices including surface roughness, friction, adhesion, scratching, wear, indentation, and lubrication.

22.2 Experimental

22.2.1 Description of AFM/FFM

AFM/FFMs used in the tribological studies have been described in several papers [10, 12, 13]. Briefly, in one of the commercial designs, the sample is mounted on a PZT tube scanner to scan the sample in the x–y-plane and to move the sample in the vertical (z) direction (Fig. 22.5). A sharp tip at the end of a flexible cantilever is

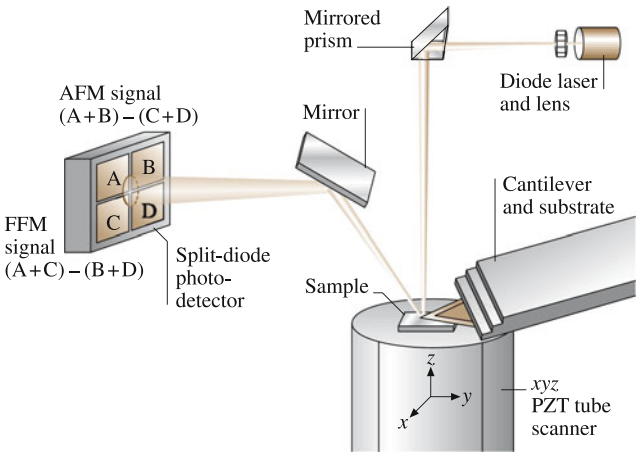

Fig. 22.5 Principles of operation of a commercial small sample AFM/FFM

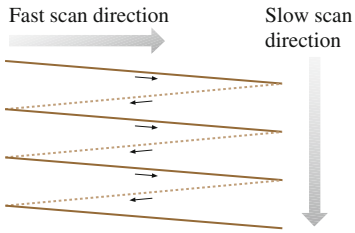

Fig. 22.6 Schematic of triangular pattern trajectory of the AFM tip as the sample is scanned in two dimensions. During imaging, data are recorded only during scans along the solid scan lines

brought in contact with the sample and the sample is scanned in a raster pattern (Fig. 22.6). Normal and frictional forces being applied at the tip–sample interface are simultaneously measured using a laser beam deflection technique. Surface roughness is measured either in the contact mode or the so-called tapping mode (intermittent contact mode). For surface roughness and friction measurements, a microfabricated square pyramidal Si_3N_4 tip with a tip radius of about 30 nm attached to a cantilever beam (with a normal beam stiffness of about 0.5 N/m) for contact mode or a square-pyramidal etched single-crystal silicon tip with a rectangular silicon cantilever beam (Fig. 22.7) is generally used at normal loads ranging from 10 to 150 nN. A preferred method of measuring friction and calibration procedures for conversion of voltages corresponding to normal and friction forces to force units, are described by Bhushan [10, 12, 13]. The samples are typically scanned over scan areas ranging from 50 nm × 50 nm to 10 μm × 10 μm, in a direction orthogonal to the long axis of the cantilever beam [14]. The scan rate is on the order of 1 Hz. For example, for this rate, the sample scanning speed would be 1 μm/s for a 500 nm × 500 nm scan area. Adhesive force measurements are performed in the so-called friction calibration mode. In this technique, the tip is brought in contact with the sample and then pulled away. The force required to pull the tip off the sample is a measure of adhesive force.

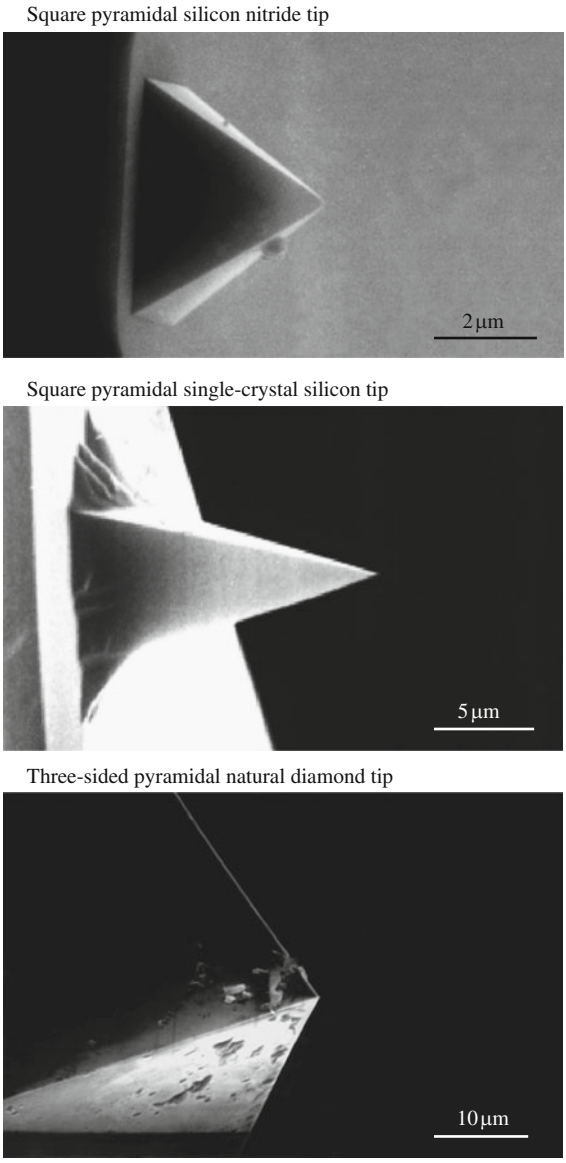

Fig. 22.7 SEM micrographs of a square-pyramidal PECVD Si_3N_4 tip with a triangular cantilever beam (*top*), a square-pyramidal etched single-crystal silicon tip with a rectangular silicon cantilever beam (*middle*), and a three-sided pyramidal natural diamond tip with a square stainless steel cantilever beam (*bottom*)

In nanoscale wear studies, the sample is initially scanned twice, typically at 10 nN to obtain the surface profile, then scanned twice at a higher load of typically 100 nN to wear and to image the surface simultaneously, and then rescanned twice at 10 nN to obtain the profile of the worn surface. For magnetic media studied by Bhushan and Ruan [15], no noticeable change in the roughness profiles was observed between the initial two scans at 10 nN and between profiles scanned at

100 nN and the final scans at 10 nN. Therefore any changes in the topography between the initial scans at 10 nN and the scans at 100 nN (or the final scans at 10 nN) are believed to occur as a result of local deformation of the sample surface. In picoindentation studies, the sample is loaded in contact with the tip. During loading, tip deflection (normal force) is measured as a function of vertical position of the sample. For a rigid sample, the tip deflection and the sample traveling distance (when the tip and sample come into contact) are equal. Any decrease in the tip deflection as compared to vertical position of the sample represents indentation. To ensure that the curvature in the tip deflection-sample traveling distance curve does not arise from PZT hysteresis, measurements on several rigid samples, including single-crystal natural diamond (IIa), were made by Bhushan and Ruan [15]. No curvature was noticed for the case of rigid samples. This suggests that any curvature for other samples should arise from the indentation of the sample.

For microscale scratching, microscale wear and nanoscale indentation hardness measurements, a three-sided pyramidal single-crystal natural diamond tip with an apex angle of 80° and a tip radius of about 100 nm (determined by scanning electron microscopy imaging) (Fig. 22.7) is used at relatively high loads (1 μN–150 μN). The diamond tip is mounted on a stainless steel cantilever beam with normal stiffness of about 25 N/m [16–19]. For scratching and wear studies, the sample is generally scanned in a direction orthogonal to the long axis of the cantilever beam (typically at a rate of 0.5 Hz). For wear studies, typically an area of 2 μm × 2 μm is scanned at various normal loads (ranging from 1 to 100 μN) for selected number of cycles. Scratching can also be performed at ramped loads [20]. For nanoindentation hardness measurements, the scan size is set to zero and then normal load is applied to make the indents. During this procedure, the diamond tip is continuously pressed against the sample surface for about two seconds at various indentation loads. Sample surface is scanned before and after the scratching, wear, or nanoindentation, to obtain the initial and the final surface topography, at a low normal load of about 0.3 μN using the same diamond tip. An area larger than the scratched, worn or indentation region is scanned to observe the scratch, wear scars, or indentation marks. Nanohardness is calculated by dividing the indentation load by the projected residual area of the indents [17]. Nanohardness and Young's modulus of elasticity (stiffness) at shallow depths as low as 5 nm are measured using a depth-sensing capacitance transducer system in an AFM [19].

Indentation experiments provide a single-point measurement of the Young's modulus of elasticity (stiffness), localized surface elasticity as well as phase contrast maps (to obtain viscoelastic properties map) can be obtained using dynamic force microscopy in which an oscillating tip is scanned over the sample surface in contact under steady and oscillating load [21–24]. Recently, a torsional resonance (TR) mode has been introduced [25, 26] which provides higher resolution. Stiffness and phase contrast maps can provide magnetic particle/polymer distributions in magnetic tapes as well as lubricant film thickness distribution.

Boundary lubrication studies are conducted using either Si_3N_4 or diamond tips [27–30]. The coefficient of friction is monitored as a function of sliding cycles.

All measurements are carried out in the ambient atmosphere (22 ± 1°C, 45 ± 5% RH, and Class 10,000).

22.2.2 Test Specimens

Data on various head slider materials and magnetic media are presented in the chapter. Al_2O_3–TiC (70 – 30 w/o) and polycrystalline and single-crystal (110) Mn–Zn ferrite are commonly used for construction of disk and tape heads. Al_2O_3, a single-phase material, is also selected for comparisons with the performance of Al_2O_3–TiC, a two-phase material. An α-type SiC is also selected which is a candidate slider material because of its high thermal conductivity and attractive machining and friction and wear properties [31]. Single crystal silicon has also been used in some head sliders but its use is discontinued [32].

Two thin-film rigid disks with polished and textured substrates, with and without a bonded perfluoropolyether are selected. These disks are 95 mm in diameter made of Al–Mg alloy substrate (1.3 mm thick) with a 10 μm thick electroless plated Ni–P coating, 75 nm thick ($Co_{79}Pt_{14}Ni_7$) magnetic coating, 20 nm thick amorphous carbon or diamondlike carbon (DLC) coating (microhardness ≈ 1,500 kg/mm^2 as measured using a Berkovich indenter), and with or without a top layer of perfluoropolyether lubricant with polar end groups (Z-DOL) coating. The thickness of the lubricant film is about 2 nm. The metal particle (MP) tape is a 12.7 mm wide and 13.2 μm thick (PET base thickness of 9.8 μm, magnetic coating of 2.9 μm with metal magnetic particles and nonmagnetic particles of Al_2O_3 and Cr_2O_3, and back coating of 0.5 μm). The barium ferrite (BaFe) tape is a 12.7 mm wide and 11 μm thick (PET base thickness of 7.3 μm, magnetic coating of 2.5 μm with barium ferrite magnetic particles and nonmagnetic particles of Al_2O_3, and back coating of 1.2 μm). Metal evaporated (ME) tape is a 12.7 mm wide tape with 10 μm thick base, 0.2 μm thick evaporated Co–Ni magnetic film and about 10 nm thick perfluoropolyether lubricant and a backcoat. PET film is a biaxially-oriented, semicrystalline polymer with particulates. Two sizes of nearly spherical particulates are generally used in the construction of PET: submicron (≈ 0.5 μm) particles of typically carbon and larger particles (2–3 μm) of silica.

22.3 Surface Roughness

Solid surfaces, irrespective of the method of formation, contain surface irregularities or deviations from the prescribed geometrical form. When two nominally flat surfaces are placed in contact, surface roughness causes contact to occur at discrete contact points. Deformation occurs at these points, and may be either elastic or plastic, depending on the nominal stress, surface roughness and material properties. The sum of the areas of all the contact points constitutes the real area that would be in contact, and for most materials at normal loads, this will be only a small fraction of the area of contact if the surfaces were perfectly smooth. In general, real area of contact must be minimized to minimize adhesion, friction and wear [12].

Characterizing surface roughness is therefore important for predicting and understanding the tribological properties of solids in contact. Various measurement techniques are used to measure surface roughness. The AFM is used to measure surface roughness on length scales from nanometers to micrometers. A second technique is noncontact optical profiler (NOP) which is a noncontact technique and does not damage the surface. The third technique is stylus profiler (SP) in which a sharp tip is dragged over the sample surface. These techniques differ in lateral resolution. Roughness plots of a glass–ceramic disk measured using an AFM (lateral resolution ≈ 15 nm), NOP (lateral resolution ≈ 1 μm) and SP (lateral resolution of ≈ 0.2 μm) are shown in Fig. 22.8a. Figure 22.8b compares the profiles of the disk obtained with different instruments at a common scale. The figures show that roughness is found at scales ranging from millimeter to nanometer scales. Measured roughness profile is dependent on the lateral and normal resolutions of the measuring instrument [33–37]. Instruments with different lateral resolutions measure features with different scale lengths. It can be concluded that a surface is composed of a large number of length of scales of roughness that are superimposed on each other.

Surface roughness is most commonly characterized by the standard deviation of surface heights which is the square roots of the arithmetic average of squares of the vertical deviation of a surface profile from its mean plane. Due to the multiscale nature of surfaces, it is found that the variances of surface height and its derivatives and other roughness parameters depend strongly on the resolution of the roughness measuring instrument or any other form of filter, hence not unique for a surface [35–38] (Fig. 22.9). Therefore, a rough surface should be characterized in a way such that the structural information of roughness at all scales is retained. It is necessary to quantify the multiscale nature of surface roughness.

An unique property of rough surfaces is that if a surface is repeatedly magnified, increasing details of roughness are observed right down to nanoscale. In addition, the roughness at all magnifications appear quite similar in structure, as qualitatively shown in Fig. 22.10. The statistical self-affinity is due to similarity in appearance of a profile under different magnifications. Such a behavior can be characterized by fractal analysis [35, 39]. The main conclusion from these studies are that a fractal characterization of surface roughness is *scale independent* and provides information of the roughness structure at all length scales that exhibit the fractal behavior.

Structure function and power spectrum of a self-affine fractal surface follow a power law and can be written as (Ganti and Bhushan model)

$$S(\tau) = C\eta^{(2D-3)}\tau^{(4-2D)}, \tag{22.1}$$

$$P(\omega) = \frac{c_1\eta^{(2D-3)}}{\omega^{(5-2D)}}, \tag{22.2a}$$

and

$$c_1 = \frac{\Gamma(5-2D)\sin[\pi(2-D)]}{2\pi}C. \tag{22.2b}$$

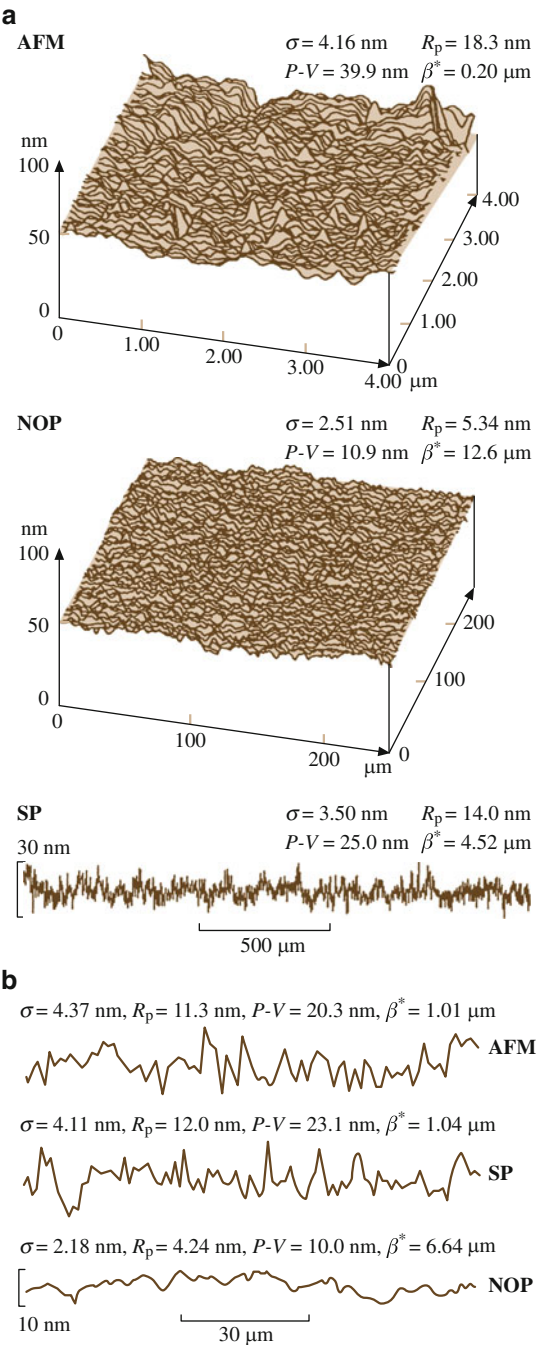

Fig. 22.8 Surface roughness plots of a glass–ceramic disk (**a**) measured using an atomic force microscope (lateral resolution ≈ 15 nm), noncontact optical profiler (NOP) (lateral resolution ≈ 1 μm) and stylus profiler (SP) with a stylus tip of 0.2 μm radius (lateral resolution ≈ 0.2 μm), and (**b**) measured using an AFM (≈ 150 nm), SP (≈ 0.2 μm), and NOP (≈ 1 μm) and plotted on a common scale [36]

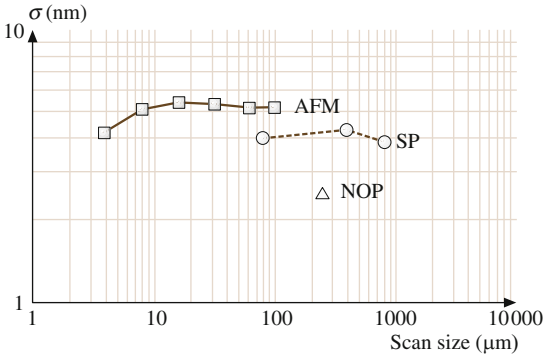

Fig. 22.9 Scale dependence of standard deviation of surface heights for a glass–ceramic disk, measured using atomic force microscope (AFM), stylus profiler (SP), and noncontact optical profiler (NOP)

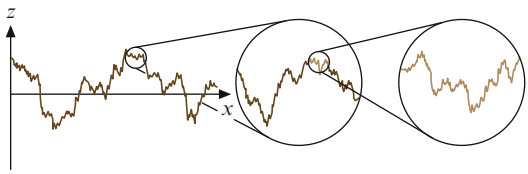

Fig. 22.10 Qualitative description of statistical self-affinity for a surface profile

The fractal analysis allows the characterization of surface roughness by two parameters D and C which are instrument-independent and unique for each surface. D (ranging from 1 to 2 for surface profile) primarily relates to relative power of the frequency contents and C to the amplitude of all frequencies. η is the lateral resolution of the measuring instrument, τ is the size of the increment (distance), and ω is the frequency of the roughness. Note that if $S(\tau)$ or $P(\omega)$ are plotted as a function of τ or ω, respectively, on a log–log plot, then the power law behavior would result into a straight line. The slope of line is related to D and the location of the spectrum along the power axis is related to C.

Figure 22.11 present the structure function of a thin-film rigid disk measured using AFM, non-contact optical profiler (NOP), and stylus profiler (SP). Horizontal shift in the structure functions from one scan to another, arises from the change in the lateral resolution. D and C values for various scan lengths are listed in Table 22.1. We note that fractal dimension of the various scans is fairly constant (1.26–1.33); however, C increases/decreases monotonically with σ for the AFM data. The error in estimation of η is believed to be responsible for variation in C. These data show that the disk surface follows a fractal structure for three decades of length scales.

Majumdar and Bhushan [40] and Bhushan and Majumdar [41] developed a fractal theory of contact between two rough surfaces. This model has been used to predict whether contacts experience elastic or plastic deformation and to predict the statistical distribution of contact points. For a review of contact models, see Bhushan [42, 43] and Bhushan and Peng [44].

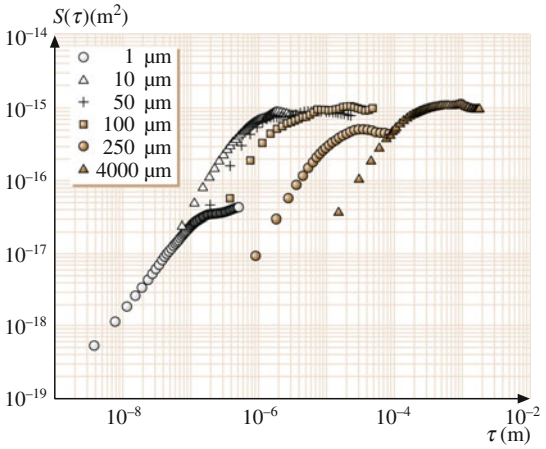

Fig. 22.11 Structure functions for the roughness data measured at various scan sizes using AFM (scan sizes: 1 μm × 1 μm, 10 μm × 10 μm, 50 μm × 50 μm, and 100 μm), NOP (scan size: 250 μm × 250 μm), and SP (scan length: 4,000 μm), for a magnetic thin-film rigid disk [35]

Table 22.1 Surface roughness parameters for a polished thin-film rigid disk

Scan size (μm × μm)	σ (nm)	D	C (nm)
1 (AFM)	0.7	1.33	9.8×10^{-4}
10 (AFM)	2.1	1.31	7.6×10^{-3}
50 (AFM)	4.8	1.26	1.7×10^{-2}
100 (AFM)	5.6	1.30	1.4×10^{-2}
250 (NOP)	2.4	1.32	2.7×10^{-4}
4,000 (NOP)	3.7	1.29	7.9×10^{-5}

AFM Atomic force microscope, *NOP* Noncontact optical profiler

Based on the fractal model of elastic–plastic contact, whether contacts go through elastic or plastic deformation is determined by a critical area which is a function of D, C, hardness and modulus of elasticity of the mating surfaces. If contact spot is smaller than the critical area, it goes through the plastic deformations and large spots go through elastic deformations. The critical contact area for inception of plastic deformation for a thin-film disk was reported by Majumdar and Bhushan [40] to be about 10^{-27} m^2, so small that all contact spots can be assumed to be elastic at moderate loads.

The question remains as to how large spots become elastic when they must have initially been plastic spots. The possible explanation is shown in Fig. 22.12. As two surfaces touch, the nanoasperities (detected by AFM type of instruments) first coming into contact have smaller radii of curvature and are therefore plastically deformed instantly, and the contact area increases. When load is increased, nanoasperities in the contact merge, and the load is supported by elastic deformation of the large scale asperities or microasperities (detected by optical profiler type of instruments) [33].

Majumdar and Bhushan [40] and Bhushan and Majumdar [41] have reported relationships for cumulative size distribution of the contact spots, portions of the real area of contact in elastic and plastic deformation modes, and the load–area relationships.

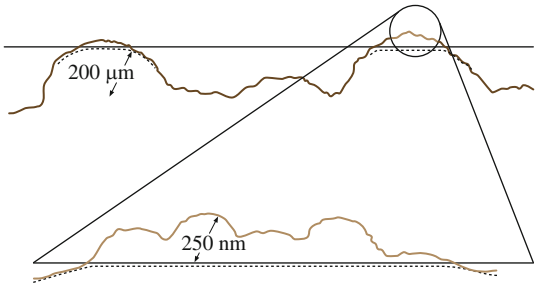

Fig. 22.12 Schematic of local asperity deformation during contact of a rough surface, upper profile measured by an optical profiler and lower profile measured by AFM, typical dimensions are shown for a polished thin-film rigid disk against a flat head slider surface [33]

22.4 Friction and Adhesion

Friction and adhesion of magnetic head sliders and magnetic media have been measured by Bhushan and Koinkar [16, 45–48], Bhushan and Ruan [15], Ruan and Bhushan [14], Bhushan et al. [27], Bhushan [2, 4, 10], Koinkar and Bhushan [28, 29, 38, 49], Kulkarni and Bhushan [50], and Li and Bhushan [51, 52], and Sundararajan and Bhushan [53].

Koinkar and Bhushan [28, 29] and Poon and Bhushan [36, 37] reported that RMS roughness and friction force increase with an increase in scan size at a given scanning velocity and normal force. Therefore, it is important that while reporting friction force values, scan sizes and scanning velocity should be mentioned. Bhushan and Sundararajan [54] reported that friction and adhesion forces are a function of tip radius and relative humidity (also see [29]). Therefore, relative humidity should be controlled during the experiments. Care also should be taken to ensure that tip radius does not change during the experiments.

22.4.1 Magnetic Head Materials

Al_2O_3–TiC is a commonly used slider material. In order to study the friction characteristics of this two phase material, friction of Al_2O_3–TiC (70 − 30 wt%) surface was measured. Figure 22.13 shows the surface roughness and friction force profiles [28]. TiC grains have a Knoop hardness of about 2,800 kg/mm^2 which is higher than that of Al_2O_3 grains of about 2,100 kg/mm^2. Therefore, TiC grains do not polish as much and result in a slightly higher elevation (about 2–3 nm higher than that of Al_2O_3 grains). Based on friction force measurements, TiC grains exhibit higher friction force than Al_2O_3 grains. The coefficients of friction of TiC and Al_2O_3 grains are 0.034 and 0.026, respectively and the coefficient of friction of Al_2O_3–TiC composite is 0.03. Local variation in friction force also arises from the scratches present on the Al_2O_3–TiC surface. Thus, local friction values of a two phase materials can be measured. Ruan and Bhushan [55] reported that local

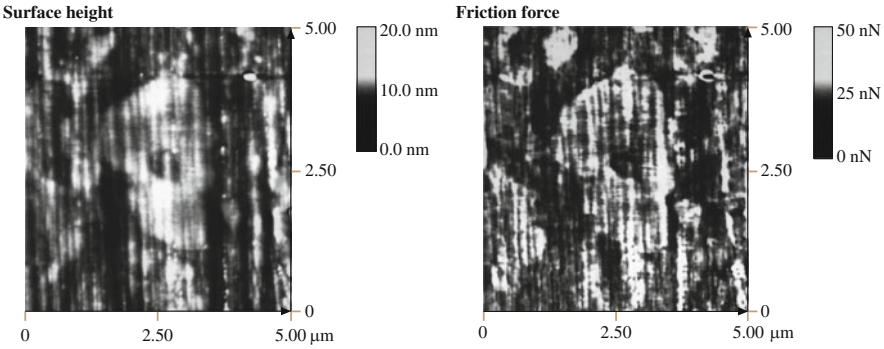

Fig. 22.13 Gray scale surface roughness ($\sigma = 0.97$ nm) and friction force map (mean = 7.0 nN, $\sigma = 0.60$ nN) for Al_2O_3–TiC (70 to 30 wt%) at a normal load of 166 nN

variation in the coefficient of friction of cleaved HOP graphite was significant which arises from structural changes occurring during the cleaving process. The cleaved HOPG surface is largely atomically smooth but exhibits line shaped regions in which the coefficient of friction is more than an order of magnitude larger. These measurements suggest that friction measurements can be used for structural mapping of the surfaces.

Surface roughness and coefficient of friction of various head slider materials were measured by Koinkar and Bhushan [29]. For typical values, see Table 22.2. Macroscale friction values for all samples are higher than microscale friction values as there is less plowing contribution in microscale measurements [10, 12, 13].

22.4.2 Magnetic Media

Bhushan and coworkers measured friction properties of magnetic media including polished and textured thin-film rigid disks, metal particle (MP), barium ferrite (BaFe) and metal evaporated (ME) tapes, and poly(ethylene terephthalate)(PET) tape substrate [2, 4, 10]. For typical values of coefficients of friction of thin-film rigid disks and MP, BaFe and ME tapes, PET tape substrate (Table 22.3). In the case of magnetic disks, similar coefficients of friction are observed for both lubricated and unlubricated disks, indicating that most of the lubricant (though partially thermally bonded) is squeezed out from between the rubbing surfaces at high interface pressures, consistent with liquids being poor boundary lubricant [13]. Coefficient of friction values on a microscale are much lower than those on the macroscale. When measured for the small contact areas and very low loads used in microscale studies, indentation hardness and modulus of elasticity are higher than at the macroscale (data to be presented later). This reduces the real area of contact and the degree of wear. In addition, the small apparent areas of contact reduces the

Table 22.2 Surface roughness (σ and P–V distance), micro- and macro-scale friction, micro-scratching/wear, and nano- and microhardness data for various samples

Sample	Surface roughness (1 μm × 1 μm)		Coefficient of friction			Scratch depth at 60 μN (nm)	Wear depth at 60 μN (nm)	Hardness	
			Microscale	Macroscale[b]				Nano	Micro at 2 mN (GPa)
	σ (nm)	P–V[a] (nm)		Initial	Final				
Al_2O_3	0.97	9.9	0.03	0.18	0.2–0.6	3.2	3.7	24.8	15.0
Al_2O_3–TiC	0.80	9.1	0.05	0.24	0.2–0.6	2.8	22.0	23.6	20.2
Polycrystalline	2.4	20.0	0.04	0.27	0.24–0.4	9.6	83.6	9.6	5.6
Mn–Zn ferrite Single-crystal (110)	1.9	13.7	0.02	0.16	0.18–0.24	9.0	56.0	9.8	5.6
Mn–Zn ferrite SiC (α-type)	0.91	7.2	0.02	0.29	0.18–0.24	0.4	7.7	26.7	21.8

[a]Peak-to-valley distance

[b]Obtained using silicon nitride ball with 3 mm diameter in a reciprocating mode at a normal load of 10 mN, reciprocating amplitude of 7 mm and average sliding speed of 1 mm/s. Initial coefficient of friction values were obtained at first cycle (0.007 m sliding distance) and final values at a sliding distance of 5 m

number of particles trapped at the interface, and thus minimize the "plowing" contribution to the friction force [8, 14, 18].

Local variations in the microscale friction of rough surfaces can be significant. Figure 22.14 shows the surface height map, the slopes of surface map taken along the sliding direction, and friction force map for a thin-film disk [8, 15, 18, 28, 38, 45–47, 56]. We note that there is no resemblance between the coefficient of friction profiles and the corresponding roughness maps, e.g., high or low points on the friction profile do not correspond to high or low points on the roughness profiles. By comparing the slope and friction profiles, we observe a strong correlation between the two. (For a clearer correlation, see gray-scale plots of slope and friction profiles for FFM tip sliding in either directions, in Fig. 22.15 to be presented in the next paragraph). We have shown that this correlation holds for various magnetic tapes, silicon, diamond, and other materials. This correlation can be explained by a "ratchet" mechanism; based on this mechanism, the local friction is a function of the local slope of the sample surface [10, 12, 13]. The friction is high at the leading edge of asperities and low at the trailing edge. In addition to the slope effect, the collision of tip encountering an asperity with a positive slope produces additional torsion of the cantilever beam leading to higher measured friction force. When encountering an asperity with a negative slope, however, there is no collision effect and hence no effect on friction. The ratchet mechanism and the collision effects thus explain the correlation between the slopes of the roughness maps and friction maps observed in Fig. 22.14.

Table 22.3 Surface roughness (σ), microscale and macro-scale friction, and nanohardness data of thin-film magnetic rigid disk, magnetic tape and magnetic tape substrate (PET) samples

Sample	σ (nm)			Coefficient of microscale friction		Coefficient of macro-scale friction		Nano-hardness (GPa)/Normal load (μN)
	NOP 250 μm × 250 μm[a]	AFM 1 μm × 1 μm[a]	10 μm × 10 μm[a]	1 μm × 1 μm[a]	10 μm × 10 μm[a]	Mn–Zn ferrite	Al_2O_3–TiC	
Polished, unlubricated disk	2.2	3.3	4.5	0.05	0.06	–	0.26	21/100
Polished, lubricated disk	2.3	2.3	4.1	0.04	0.05	–	0.19	–
Textured, lubricated disk	4.6	5.4	8.7	0.04	0.05	–	0.16	–
Metal-particle tape	6.0	5.1	12.5	0.08	0.06	0.19	–	0.30/50
Barium-ferrite tape	12.3	7.0	7.9	0.07	0.03	0.18	–	0.25/25
Metal-evaporated tape	9.3	4.7	5.1	0.05	0.03	0.18	–	0.7 to 4.3/75
PET tape substrate	33	5.8	7.0	0.05	0.04	0.55	–	0.3/20 and 1.4/20[b]

[a]Scan area; *NOP* Noncontact optical profiler; *AFM* Atomic force microscope
[b]Numbers are for polymer and particulate regions, respectively

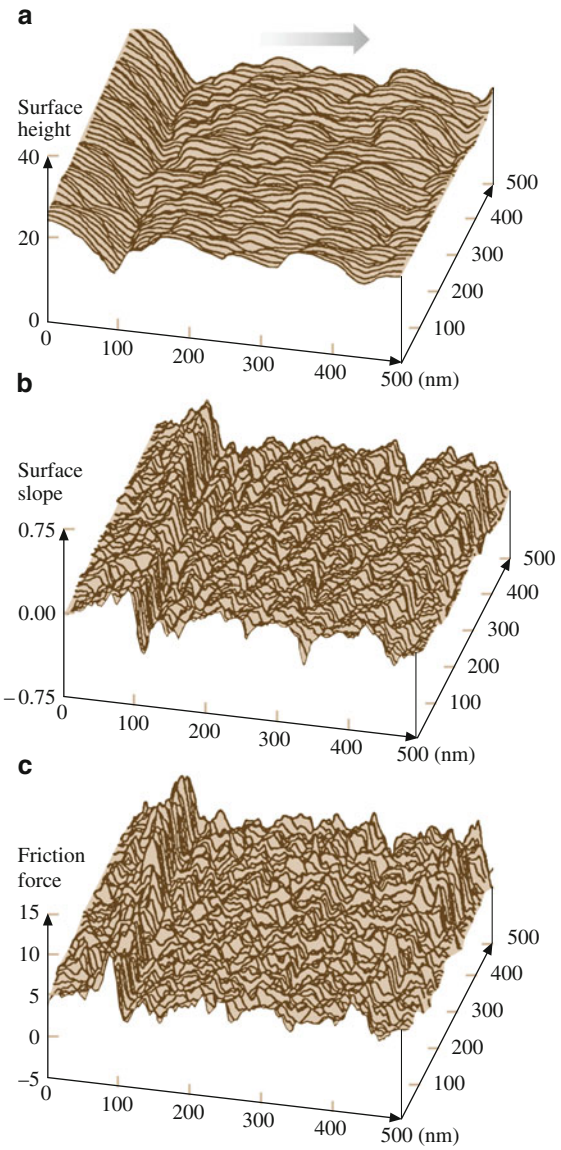

Fig. 22.14 (**a**) Surface height map ($\sigma = 4.4$ nm), (**b**) slope of the roughness profiles taken in the sample sliding direction (the *horizontal axis*) (mean = 0.023, $\sigma = 0.18$), and (**c**) friction force map (mean = 6.2 nN, $\sigma = 2.1$ nN) for a textured thin-film rigid disk at a normal load of 160 nN [18]

To study the directionality effect on the friction, gray scale plots of coefficients of local friction of the thin-film disk as the FFM tip is scanned in either direction are shown in Fig. 22.15. Corresponding gray scale plots of slope of roughness maps are also shown in Fig. 22.15. The left hand set of the figures corresponds to

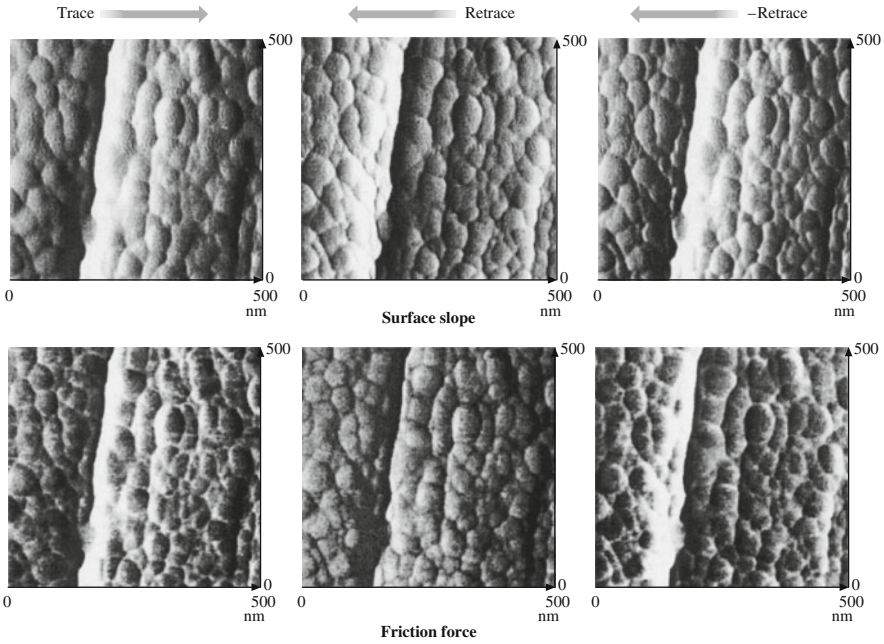

Fig. 22.15 Gray-scale plots of the slope of the surface roughness and the friction force maps for a textured thin-film rigid disk with FFM tip sliding in different directions. *Higher points* are shown by *lighter color*

the tip sliding from the left towards right (trace direction), and the middle set corresponds to the tip sliding from the right towards left (retrace direction). It is important to take into account the sign change of surface slope and friction force which occur in the trace and retrace directions. In order to facilitate comparison of directionality effect on friction, the last set of the figures in the right hand column show the data with sign of surface slope and friction data in the retrace direction reversed. Now we compare trace and -retrace data. It is clear that the friction experienced by the tip is dependent upon the scanning direction because of surface topography.

The directionality effect in friction on a macroscale is generally averaged out over a large number of contacts. It has been observed in some magnetic tapes. In a macro-scale test, a 12.7 mm wide MP tape was wrapped over an aluminium drum and slid in a reciprocating motion with a normal load of 0.5 N and a sliding speed of about 60 mm/s. Coefficient of friction as a function of sliding distance in either direction is shown in Fig. 22.16. We note that coefficient of friction on a macro-scale for this tape is different in different directions.

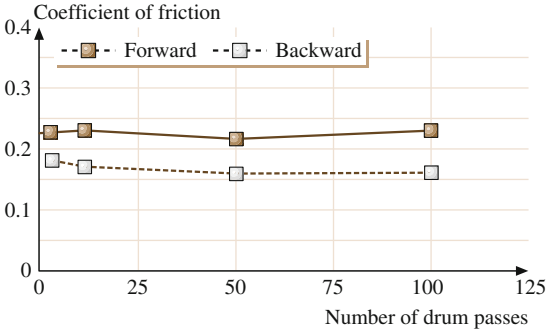

Fig. 22.16 Coefficient of macro-scale of friction as a function of sliding cycles for a metal-particle (MP) tape sliding over an aluminium drum in a reciprocating mode in both directions. Normal load = 0.5 N over 12.7 mm wide tape, sliding speed = 60 mm/s [7]

22.5 Scratching and Wear

22.5.1 Nanoscale Wear

Bhushan and Ruan [15] conducted nanoscale wear tests on MP tapes at a normal load of 100 nN. Figure 22.17 shows the topography of the MP tape obtained at two different loads. For a given normal load, measurements were made twice. There was no discernible difference between consecutive measurements for a given normal load. However, as the load increased from 10 to 100 nN, topographical changes were observed; material (indicated by an arrow) was pushed toward the right side in the sliding direction of the AFM tip relative to the sample. The material movement is believed to occur as a result of plastic deformation of the tape surface. Similar behavior was observed on all tapes studied. Magnetic tape coating is made of magnetic particles and polymeric binder. Any movement of the coating material can eventually lead to loose debris. Debris formation is an undesirable situation as it may contaminate the head which may increase friction and/or wear between the head and tape, in addition to the deterioration of the tape itself. With disks, they did not notice any deformation under a 100 nN normal load.

22.5.2 Microscale Scratching

Microscratches have been made on various potential head slider materials (Al_2O_3, Al_2O_3–TiC, Mn–Zn ferrite and SiC), and various magnetic media (unlubricated polished thin-film disk, MP, BaFe, ME tapes, and PET substrates) and virgin, treated and coated Si(111) wafers at various loads [16, 18, 28, 45–49, 53, 57, 58]. As mentioned earlier, the scratches are made using a diamond tip.

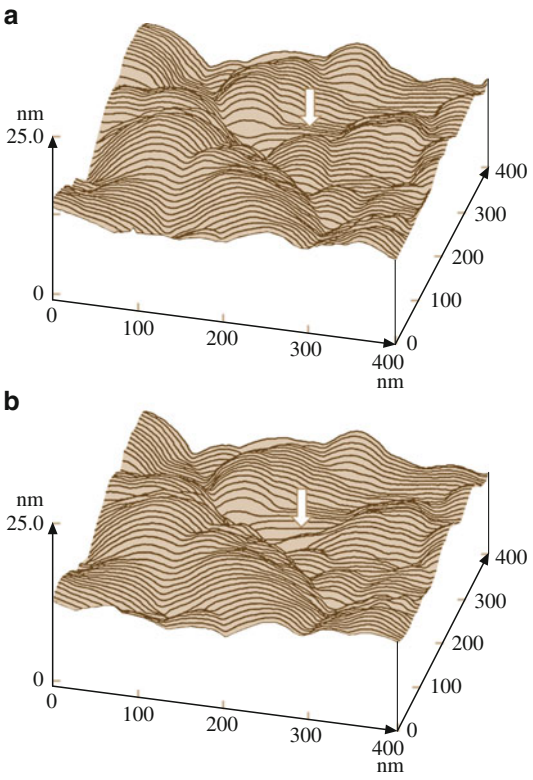

Fig. 22.17 Surface roughness maps of a metal-particle (MP) tape at applied normal load of (**a**) 10 nN and (**b**) 100 nN. Location of the change in surface topography as a result of nanowear is indicated by *arrows* [15]

Magnetic Head Materials

Scratch depths as a function of load and representative scratch profiles with corresponding 2D gray scale plots at various loads after a single pass (unidirectional scratching) for Al_2O_3, Al_2O_3–TiC, polycrystalline and single-crystal Mn–Zn ferrite and SiC are shown in Figs. 22.18 and 22.19, respectively. Variation in the scratch depth along the scratch is about $\pm 15\%$. The Al_2O_3 surface could be scratched at a normal load of 40 μN. The surface topography of polycrystalline Al_2O_3 shows the presence of porous holes on the surface. The 2D gray scale plot of scratched Al_2O_3 surface shows one porous hole between scratches made at normal loads of 40 μN and 60 μN. Regions with defects or porous holes present, exhibit lower scratch resistance (see region marked by the arrow on 2D gray scale plot of Al_2O_3). The Al_2O_3–TiC surface could be scratched at a normal load of 20 μN. The scratch resistance for TiC grains is higher than that of Al_2O_3 grains. The scratches generated at normal loads of 80 μN and 100 μN show that scratch depth of Al_2O_3 grains is higher than that of TiC grains (see corresponding gray scale plot for Al_2O_3–TiC). Polycrystalline and single-crystal Mn–Zn ferrite could be scratched at a normal load of 20 μN. The scratch width is much larger for the ferrite specimens as

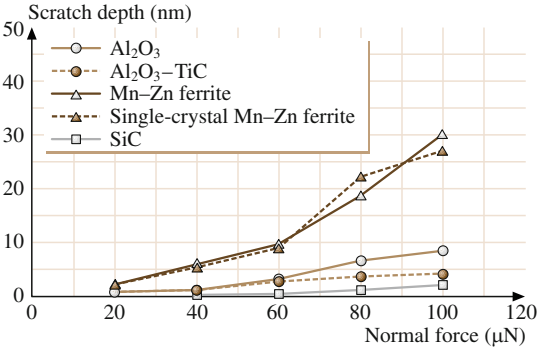

Fig. 22.18 Scratch depth as a function of normal load after one unidirectional cycle for Al_2O_3, Al_2O_3–TiC, polycrystalline Mn–Zn ferrite, single-crystal Mn–Zn ferrite and SiC [28]

compared with other specimens. For SiC, there is no measurable scratch observed at a normal load of 20 μN. At higher normal loads, very shallow scratches are produced. Table 22.2 presents average scratch depth at 60 μN normal load for all specimens. SiC has the highest scratch resistance followed by Al_2O_3–TiC, Al_2O_3 and polycrystalline and single-crystal Mn–Zn ferrite. Polycrystalline and single-crystal Mn–Zn ferrite specimens exhibit comparable scratch resistance.

Magnetic Media

Scratch depths as a function of load and scratch profiles at various loads after ten scratch cycles for unlubricated, polished disk and MP tape are shown in Figs. 22.20 and 22.21. We note that scratch depth increases with an increase in the normal load. Tape could be scratched at about 100 nN. With disk, gentle scratch marks under 10 μN load were barely visible. It is possible that material removal did occur at lower load on an atomic scale which was not observable with a scan size of 5 μm square. For disk, scratch depth at 40 μN is less than 10 nm deep. The scratch depth increased slightly at the load of 50 μN. Once the load is increased in excess of 60 μN, the scratch depth increased rapidly. These data suggest that the carbon coating on the disk surface is much harder to scratch than the underlying thin-film magnetic film. This is expected since the carbon coating is harder than the magnetic material used in the construction of the disks.

Microscratch characterization of ultrathin amorphous carbon coatings, deposited by filtered cathodic arc (FCA) direct ion beam (IB), electron cyclotron resonance plasma chemical vapor deposition (ECR-CVP), and sputter (SP) deposition processes have been conducted using a nanoindenter and an AFM [20, 48, 49, 51–53, 59]. Data on various coatings of different thicknesses using a Berkovich tip are compared in Fig. 22.22. Critical loads for various coatings and silicon substrate are summarized in Fig. 22.23. It is clear that, for all deposition methods, the critical load increases with increasing coating thickness due to better load-carrying capacity of thicker coatings as compared to the thinner ones. In comparison of the

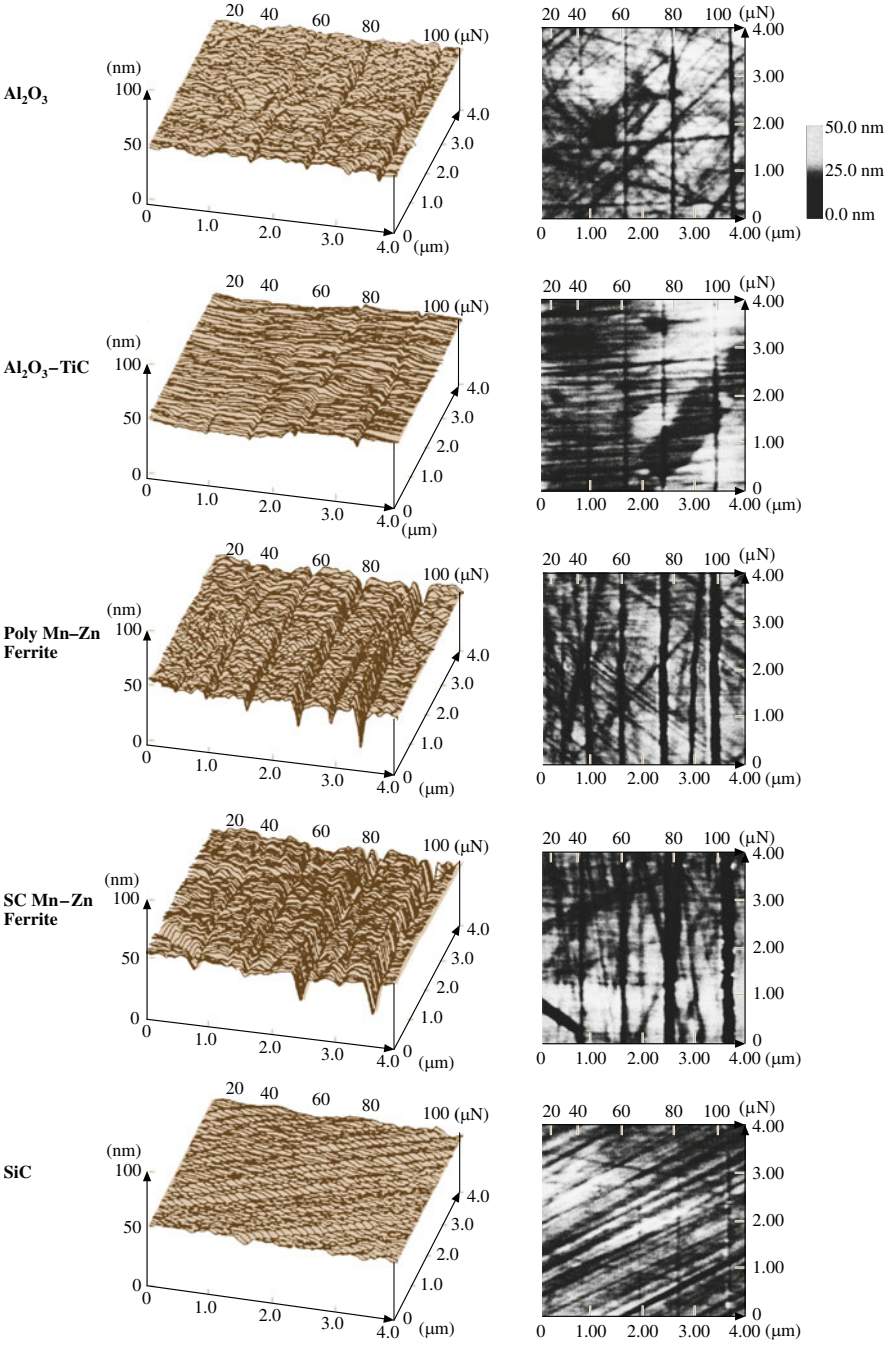

Fig. 22.19 Surface profiles (*left column*) and 2D gray scale plots (*right column*) of scratched Al_2O_3, Al_2O_3–TiC, polycrystalline Mn–Zn ferrite, single-crystal Mn–Zn ferrite, and SiC surfaces. Normal loads used for scratching for one unidirectional cycle are listed in the figure [28]

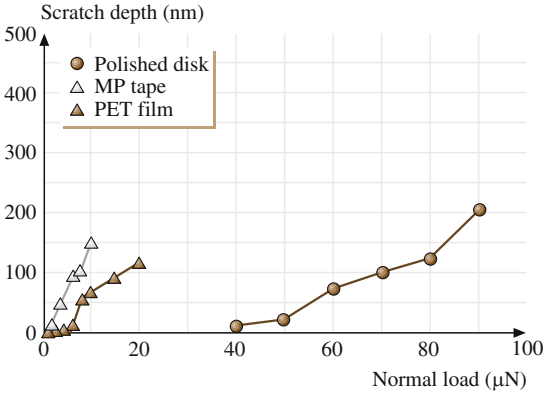

Fig. 22.20 Scratch depth as a function of normal load after ten scratch cycles for unlubricated polished thin-film rigid disk, MP tape and PET film [18, 45, 47]

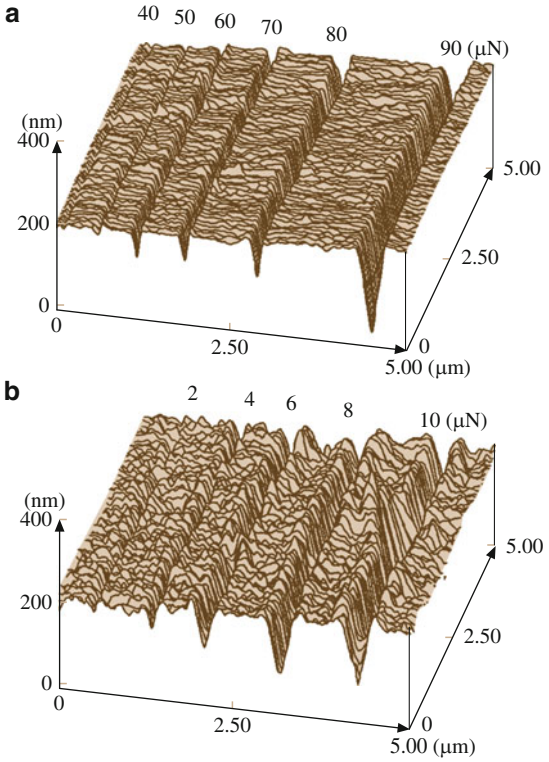

Fig. 22.21 Surface profiles for scratched (**a**) unlubricated polished thin-film rigid disk and (**b**) MP tape. Normal loads used for scratching for ten cycles are listed in the figure [18]

different deposition methods, ECR-CVD and FCA coatings show superior scratch resistance at 20- and 10 nm thicknesses compared to SP coatings. As the coating thickness reduces, ECR-CVD exhibits the best scratch resistance followed by FCA and SP coatings.

Since tapes scratch readily, for comparisons in scratch resistance of various tapes, Bhushan and Koinkar [47] made scratches on selected three tapes only with one cycle. Figure 22.24 presents the scratch depths as a function of normal load after one cycle for three tapes – MP, BaFe and ME tapes. For the MP and BaFe particulate tapes, Bhushan and Koinkar [47] noted that the scratch depth along

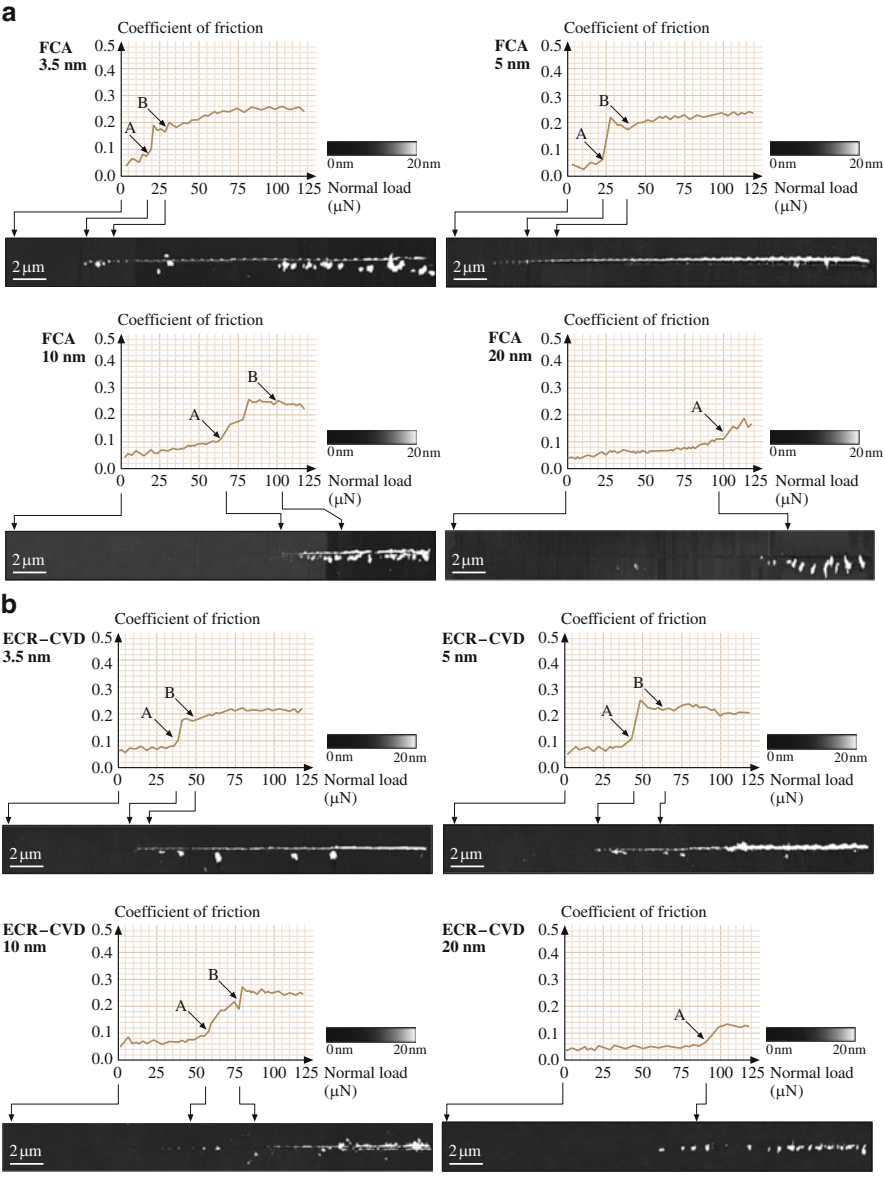

Fig. 22.22 (continued)

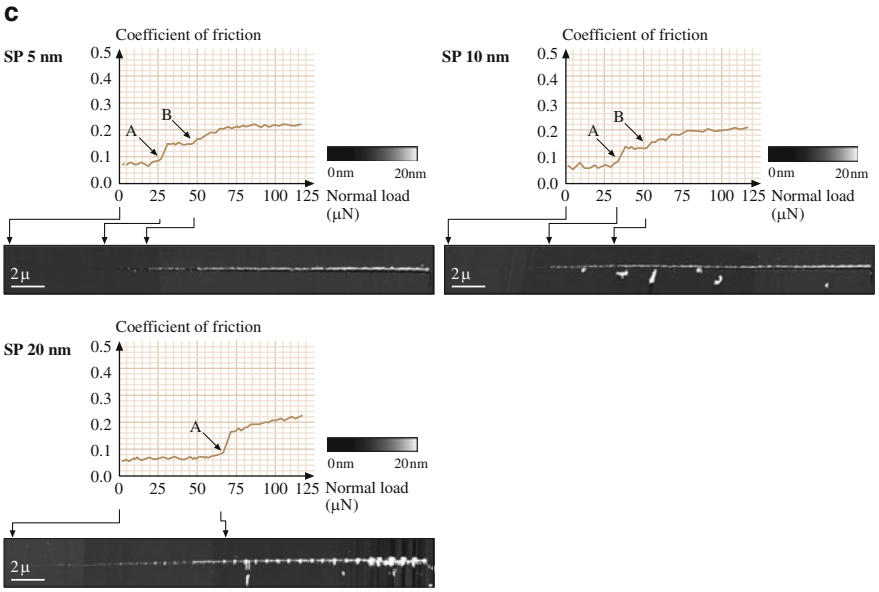

Fig. 22.22 Coefficient of Friction profiles during scratch as a function of normal load and corresponding AFM surface height images for (**a**) FCA, (**b**) ECR-CVD, and (**c**) SP-coatings [20]

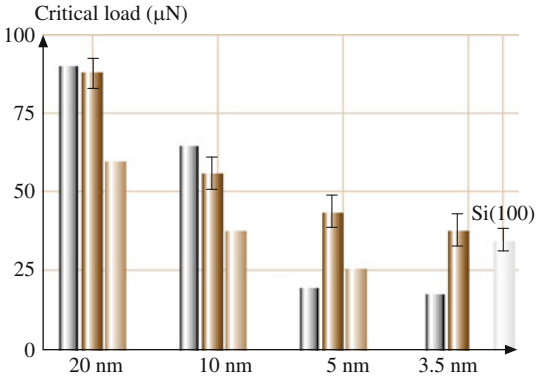

Fig. 22.23 Summary of critical loads estimated from the coefficient of friction profiles and AFM images [20]

(parallel) and across (perpendicular) the longitudinal direction of the tapes is similar. Between the two tapes, MP tape appears to be more scratch resistant than BaFe tape, which depends on the binder, pigment volume concentration (PVC) and the head cleaning agent (HCA) contents. ME tapes appear to be much more scratch resistant than the particulate tapes. However, the ME tape breaks up catastrophically in a brittle mode at a normal load higher than the 50 μN (Fig. 22.25), as

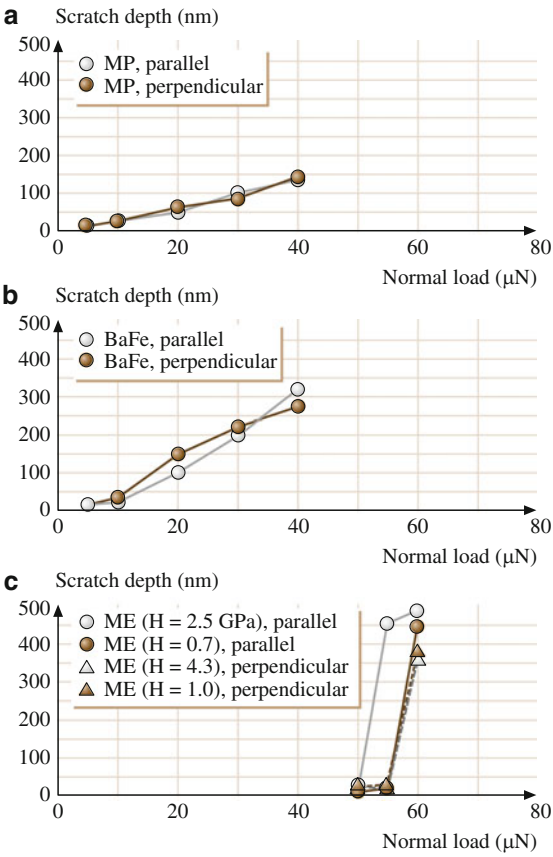

Fig. 22.24 Scratch depth as a function of normal load after one scratch cycle for (**a**) MP, (**b**) BaFe, and (**c**) ME tapes along parallel and perpendicular directions with respect to the longitudinal axis of the tape [47]

compared to particulate tapes in which the scratch rate is constant. They reported that the hardness of ME tapes is higher than that of particulate tapes, however, a significant difference in the nanoindentation hardness values of the ME film from region to region (Table 22.3) was observed. They systematically measured scratch resistance in the high and low hardness regions along and across the longitudinal directions. Along the parallel direction, load required to crack the coating was lower (implying lower scratch resistance) for a harder region, than that for a softer region. The scratch resistance of high hardness region along the parallel direction is slightly poorer than that for along perpendicular direction. Scratch widths in both low and high hardness regions is about half ($\approx$ 2 μm) than that in perpendicular direction ($\approx$ 1 μm). In the parallel direction, the material is removed in the form of chips and lateral cracking also emanates from the wear zone. ME films have columnar structure with the columns lined up with an oblique angle of on the order of about 35° with respect to the normal to the coating surface [3, 60]. The

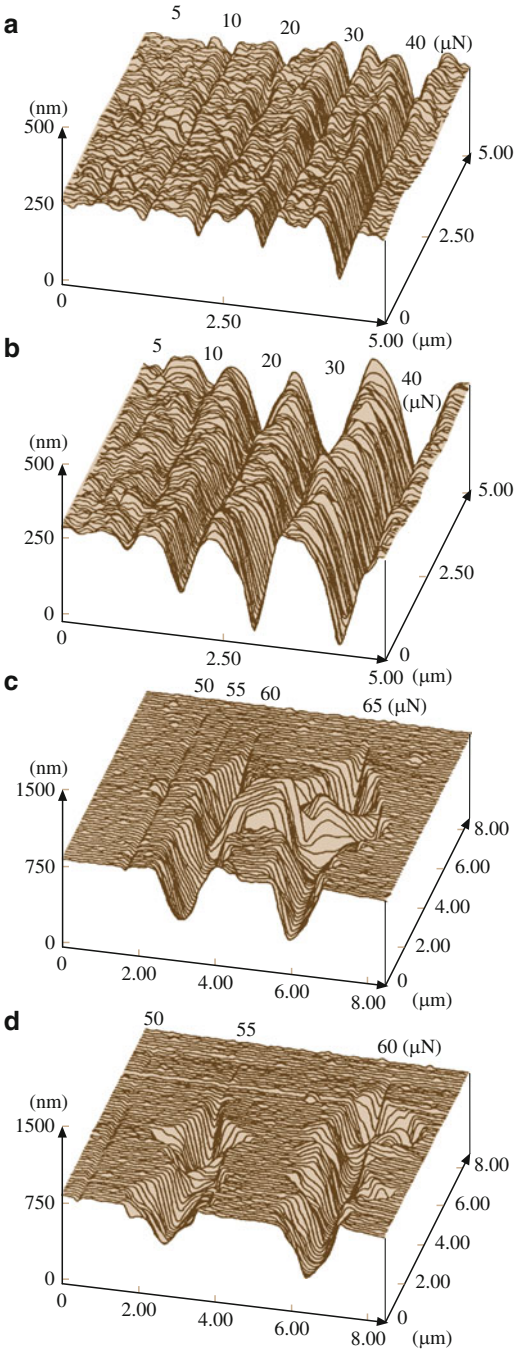

Fig. 22.25 Surface maps for scratched (**a**) MP, (**b**) BaFe, (**c**) ME (H = 0.7 GPa), and (**d**) ME (H = 2.5 GPa) tapes along parallel direction. Normal loads used for scratching for one cycle are listed in the figure [47]

column orientation may be responsible for directionality effect on the scratch resistance. Hibst [60] have reported the directionality effect in the ME tape-head wear studies. They have found that the wear rate is lower when the head moves in the direction corresponding to the column orientation than in the opposite direction.

PET films could be scratched at loads of as low as about 2 μN (Fig. 22.26). Figure 22.26a shows scratch marks made at various loads. Scratch depth along the scratch does not appear to be uniform. This may occur because of variations in the mechanical properties of the film. Bhushan and Koinkar [45] also conducted scratch studies in the selected particulate regions. Scratch profiles at increasing loads in the particulate region are shown in Fig. 22.26b. We note that the bump (particle) is barely scratched at 5 μN and it can be scratched readily at higher loads. At 20 μN, it essentially disappears.

22.5.3 Microscale Wear

By scanning the sample (in 2D) while scratching, wear scars are generated on the sample surface [16, 18, 28, 45–49, 53, 54, 57, 58]. The major benefit of a single cycle wear test over a scratch test is that wear data can be obtained over a large area.

Magnetic Head Materials

Figure 22.27 shows the wear depth as a function of load for one cycle for different slider materials. Variation in the wear depth in the wear mark is dependent upon the material. It is generally within ±5%. The mean wear depth increases with the increase in normal load. The representative surface profiles showing the wear marks

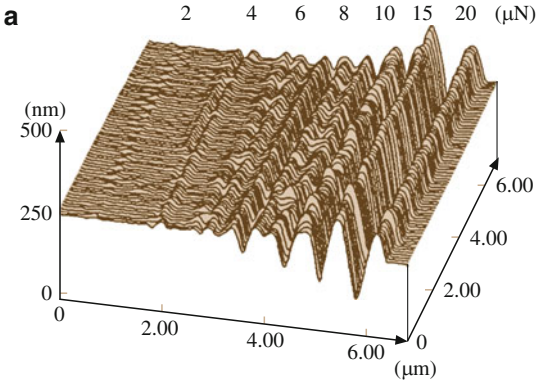

Fig. 22.26 (continued)

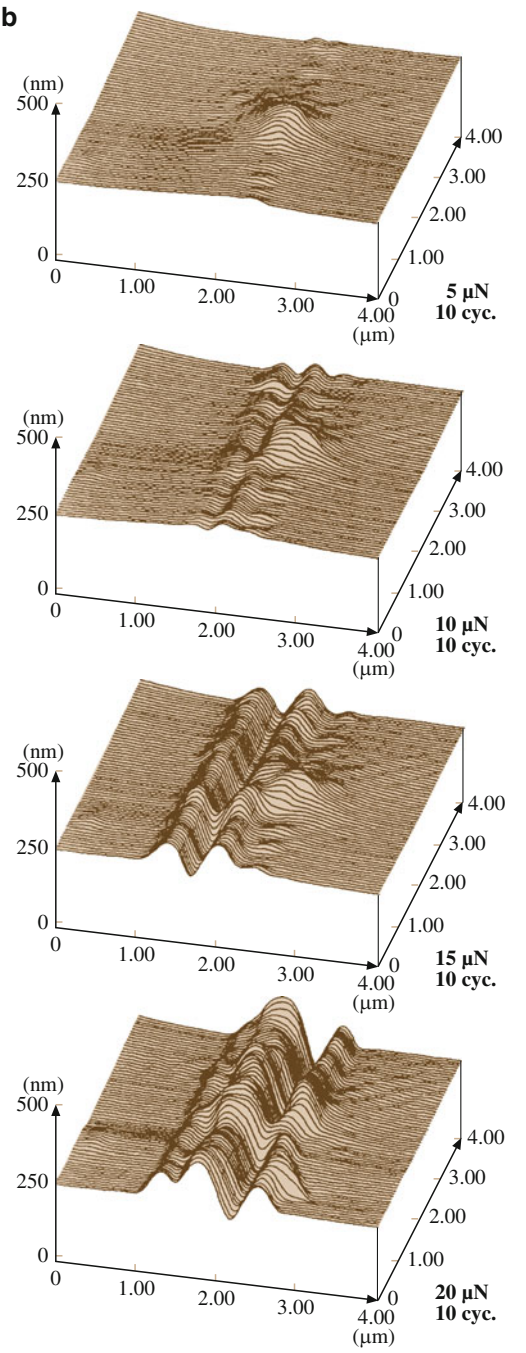

Fig. 22.26 Surface profiles for scratched PET film (**a**) polymer region, (**b**) ceramic particulate region. The loads used for various scratches at ten cycles are indicated in the plots [45]

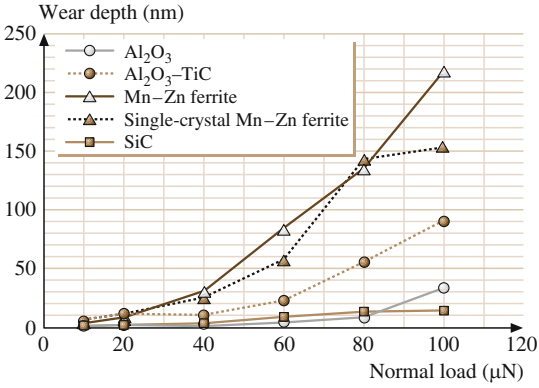

Fig. 22.27 Wear depth as a function of normal load after one scan cycle for Al_2O_3, Al_2O_3–TiC, polycrystalline Mn–Zn ferrite, single-crystal Mn–Zn ferrite and SiC [28]

(central 2 μm × 2 μm region) at a normal load of 60 μN for all specimens are shown in Fig. 22.28. The material is removed uniformly in the wear region for all specimens. Table 22.2 presents average wear depth at 60 μN normal load for all specimens. Microwear resistance of SiC and Al_2O_3 is the highest followed by Al_2O_3–TiC, single-crystal and polycrystalline Mn–Zn ferrite.

Next, wear experiments were conducted for multiple cycles. Figure 22.29 shows the 2D gray scale plots and corresponding section plot (on tope of each gray scale plot), taken at a location shown by an arrow for Al_2O_3 (left column) and Al_2O_3–TiC (right column) specimen obtained at a normal load of 20 μN and at a different number of scan cycles. The central regions (2 μm × 2 μm) show the wear mark generated after a different number of cycles. Note the difference in the vertical scale of gray scale and section plots. The Al_2O_3 specimen shows that wear initiates at the porous holes or defects present on the surface. Wear progresses at these locations as a function of number of cycles. In the porous hole free region, microwear resistance is higher. In the case of the Al_2O_3–TiC specimen for about five scan cycles, the microwear resistance is higher at the TiC grains and is lower at the Al_2O_3 grains. The TiC grains are removed from the wear mark after five scan cycles. This indicates that microwear resistance of multi-phase materials depends upon the individual grain properties. Evolution of wear is uniform within the wear mark for ferrite specimens. Figure 22.30 shows plot of wear depth as a function of number of cycles at a normal load of 20 μN for all specimens. The Al_2O_3 specimen reveals highest microwear resistance followed by SiC, Al_2O_3–TiC, polycrystalline and single-crystal Mn–Zn ferrite. Wear resistance of Al_2O_3–TiC is inferior to that of Al_2O_3. Chu et al. [61] studied friction and wear behavior of the single-phase and multi-phase ceramic materials and found that wear resistance of multi-phase materials was poorer than single-phase materials. Multi-phase materials have more material flaws than the single-phase material. The differences in thermal and mechanical properties between the two phases may lead to cracking during processing, machining or use.

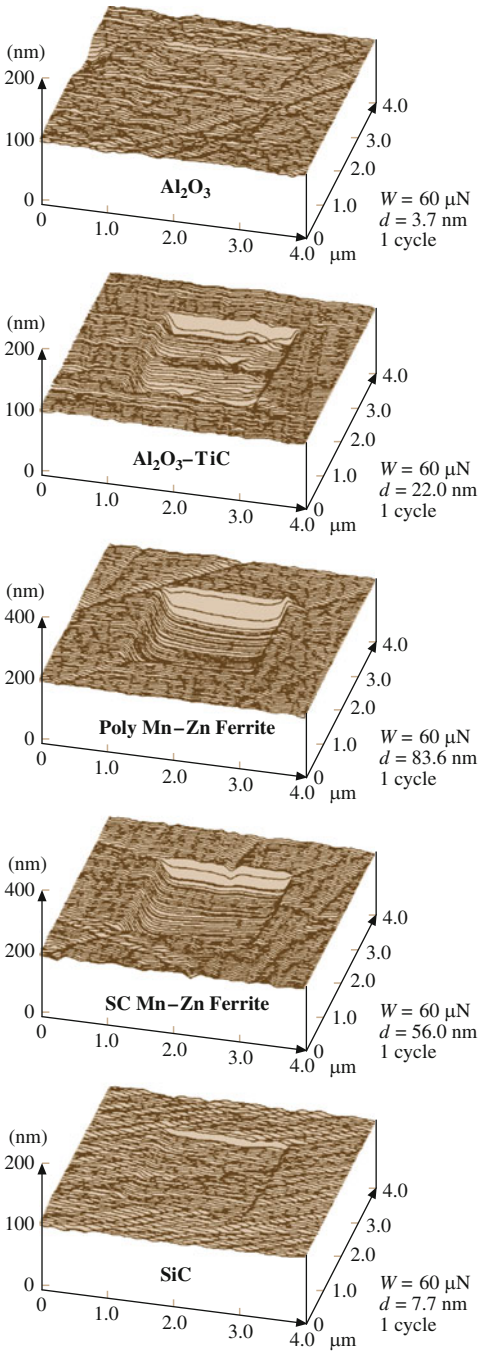

Fig. 22.28 Surface profiles showing the worn region (center 2 μm × 2 μm) after one scan cycles at a normal load of 60 μN for Al_2O_3, Al_2O_3–TiC, polycrystalline Mn–Zn ferrite, single-crystal Mn–Zn ferrite and SiC [28]

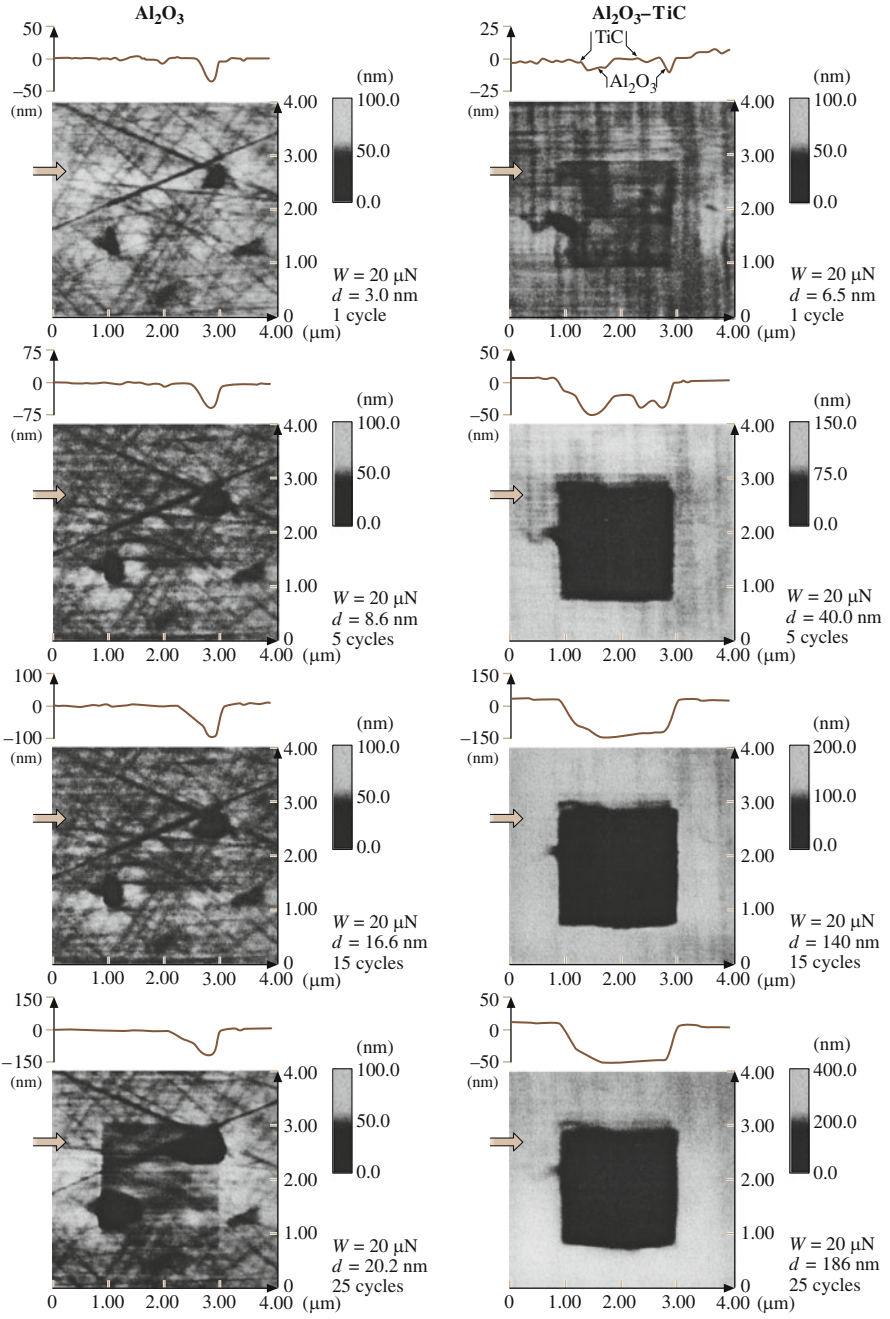

Fig. 22.29 Gray scale 2D plots showing the worn region (center 2 μm × 2 μm) at a normal load of 20 μN and different number of scan cycles for Al_2O_3 and Al_2O_3–TiC. The 2D section plots taken at a location shown by an arrow are shown on the top of corresponding gray scale plot. Note the change in vertical scale for gray scale and 2D section plots [28]

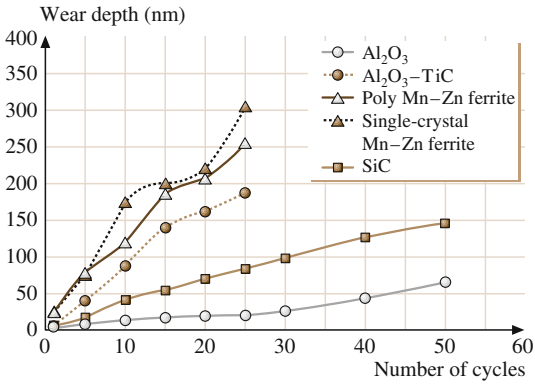

Fig. 22.30 Wear depth as a function of number of cycles at a normal load of 20 μN for Al_2O_3, Al_2O_3–TiC, polycrystalline Mn–Zn ferrite, single-crystal (SC) Mn–Zn ferrite and SiC [28]

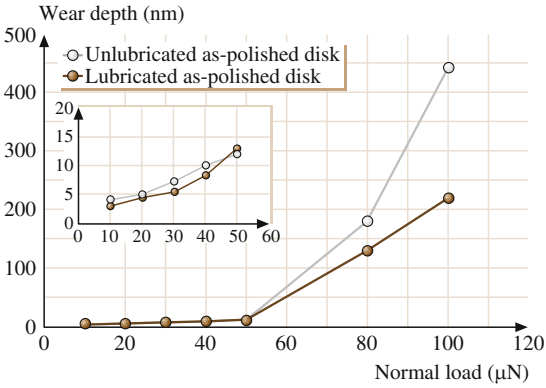

Fig. 22.31 Wear depth as a function of normal load for polished, lubricated and unlubricated thin-film rigid disks after one cycle [18]

Magnetic Media

Figure 22.31 shows the wear depth as a function of load for one cycle for the polished, unlubricated and lubricated disks [18]. Figure 22.32 shows profiles of the wear scars generated on unlubricated disk. The normal force for the imaging was about 0.5 μN and the loads used for the wear were 20, 50, 80 and 100 μN as indicated in the figure. We note that wear takes place relatively uniformly across the disk surface and essentially independent of the lubrication for the disks studied. For both lubricated and unlubricated disks, the wear depth increases slowly with load at low loads with almost the same wear rate. As the load is increased to about 60 μN, wear increases rapidly with load. The wear depth at 50 μN is about 14 nm, slightly less than the thickness of the carbon film. The rapid increase of wear with load at loads larger than 60 μN is an indication of the breakdown of the carbon coating on the disk surface.

Figure 22.33 shows the wear depth as a function of number of cycles for the polished disks (lubricated and unlubricated). Again, for both unlubricated and

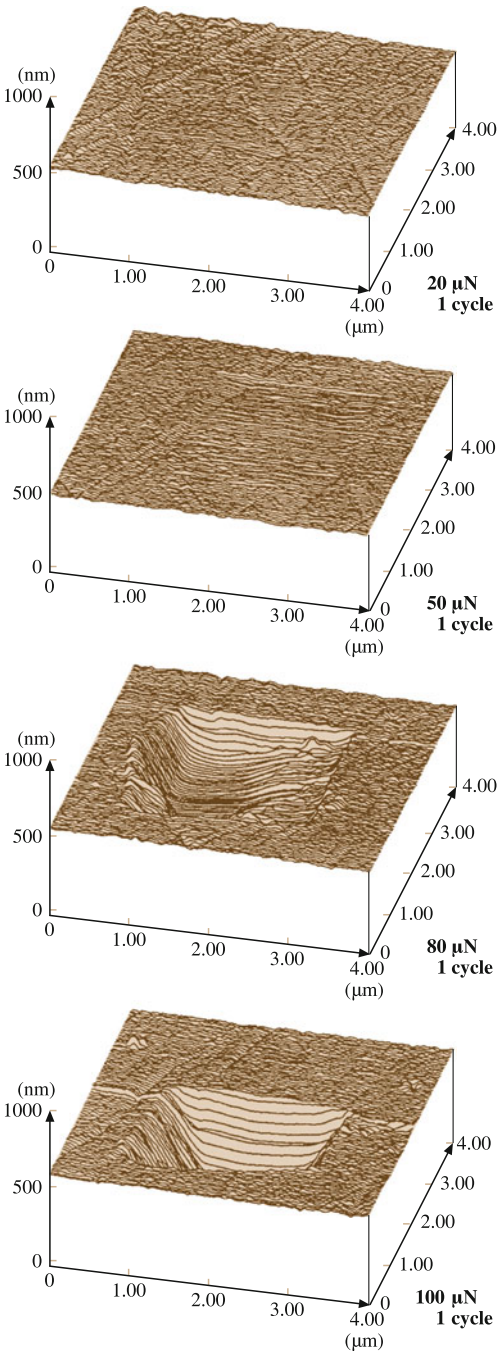

Fig. 22.32 Surface maps of a polished, unlubricated thin-film rigid disk showing the worn region (center 2 μm × 2 μm) after one cycle. The normal loads are indicted in the figure [18]

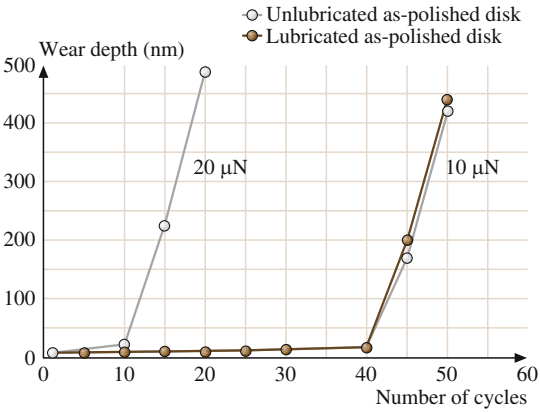

Fig. 22.33 Wear depth as a function of number of cycles for polished, lubricated and unlubricated thin-film rigid disks at 10 μN and for polished, unlubricated disk at 20 μN [18]

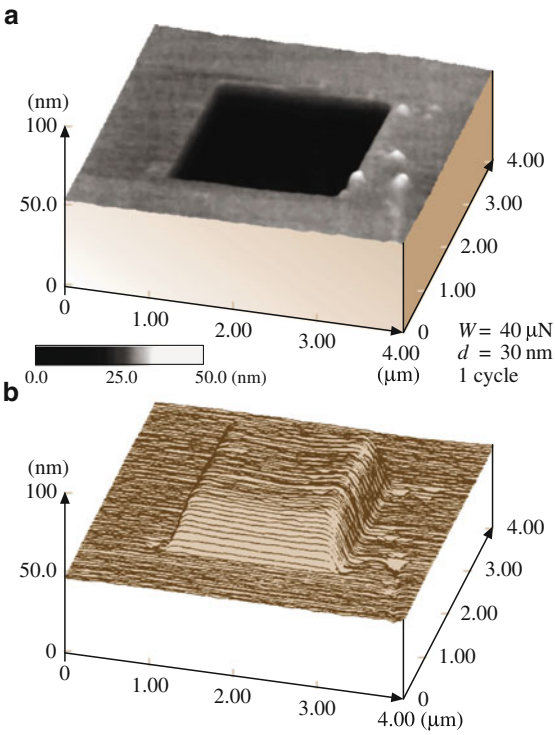

Fig. 22.34 Surface maps of a polished, unlubricated thin-film rigid disk showing the worn region (center 2 μm × 2 μm) at 20 μN. The number of cycles are indicated in the figure [18]

lubricated disks, wear initially takes place slowly with a sudden increase between 40 and 50 cycles at 10 μN. The sudden increase occurred after 10 cycles at 20 μN. This rapid increase is associated with the breakdown of the carbon coating. The wear profiles at various cycles are shown in Fig. 22.34 for a polished, unlubricated

disk at a normal load of 20 μN. Wear is not uniform and the wear is largely initiated at the texture grooves present on the disk surface. This indicates that surface defects strongly affect the wear rate.

Hard amorphous carbon coatings are used to provide wear and corrosion resistance to magnetic disks and MR/GMR magnetic heads. A thick coating is desirable for long durability; however, to achieve ever increasing high recording densities, it is necessary to use as thin a coating as possible. Microwear data on various amorphous carbon coatings of different thicknesses have been conducted by Bhushan and Koinkar [48], Koinkar and Bhushan [49], and Sundararajan and Bhushan [53]. Figure 22.35 shows a wear mark on an uncoated Si(100) and various 10 nm thick carbon coatings. It is seen that Si(100) wears uniformly, whereas carbon coatings wear nonuniformly. Carbon coating failure is sudden and accompanied by a sudden rise in friction force. Figure 22.36 shows the wear depth of Si(100) substrate and various coatings at two different loads. FCA and ECR-CVD, 20 nm thick coatings show excellent wear resistance up to 80 μN, the load that is required for the IB 20 nm coating to fail. In these tests, failure of a coating results when the wear depth exceeds the quoted coating thickness. The SP 20 nm coating fails at the much lower load of 35 μN. At 60 μN, the coating hardly provides any protection. Moving on to the 10 nm coatings, ECR-CVD coating requires about

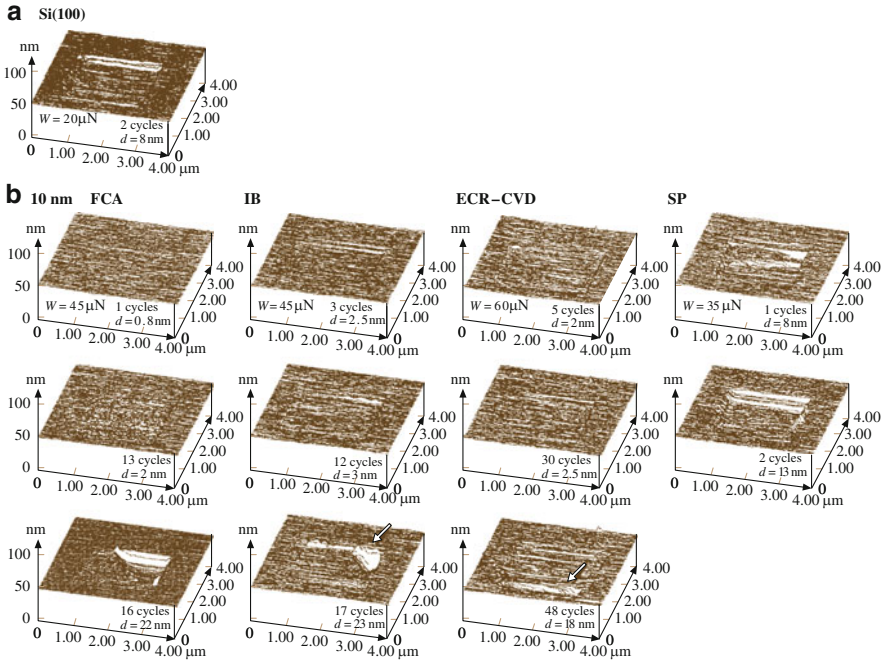

Fig. 22.35 AFM images of wear marks on (**a**) bare Si(100), and (**b**) all 10 nm thick amorphous carbon coatings [53]

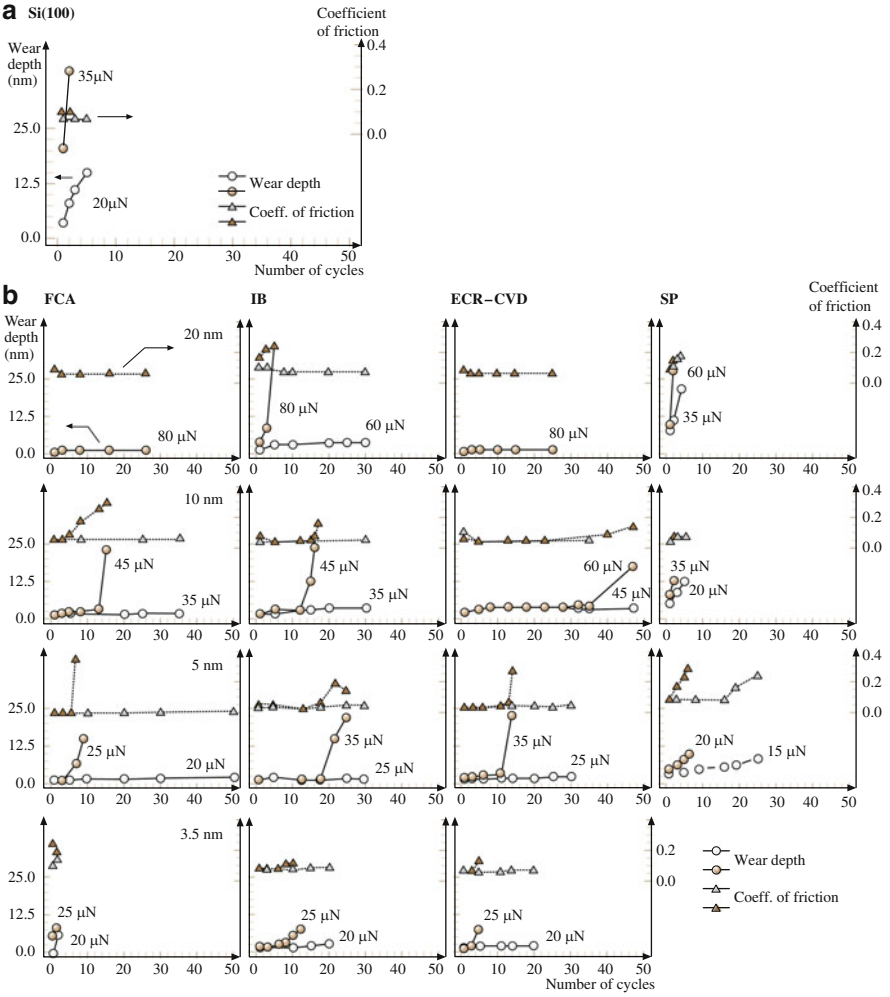

Fig. 22.36 Wear data of (**a**) bare Si(100) and (**b**) all amorphous carbon coatings. Coating thickness is constant along each row in (**b**). Both wear depth and coefficient of friction during wear for a given cycle are plotted [53]

40 cycles at 60 μN to fail as compared to IB and FCA, which fail at 45 μN. the FCA coating exhibits slight roughening in the wear track after the first few cycles, which leads to an increase in the friction force. The SP coating continues to exhibit poor resistance, failing at 20 μN. For the 5 nm coatings, the load required to fail the coatings continues to decrease. But IB and ECR-CVD still provide adequate protection as compared to bare Si(100) in that order, failing at 35 μN compared to FCA at 25 μN and SP at 20 μN. Almost all the 20, 10, and 5 nm coatings provide better wear resistance than bare silicon. At 3.5 nm, FCA coating provides no wear

resistance, failing almost instantly at 20 μN. The IB and ECR-CVD coating show good wear resistance at 20 μN compared to bare Si(100). But IB lasts only about 10 cycles and ECR-CVD about 3 cycles at 25 μN.

The wear tests highlight the differences in the coatings more vividly than the scratch tests data presented earlier. At higher thicknesses (10 and 20 nm), the ECR-CVD and FCA coatings appear to show the best wear resistance. This is probably due to higher hardness of the coatings (see data presented later). At 5 nm, IB coating appears to be the best. FCA coatings show poorer wear resisting with decreasing coating thickness. SP coatings showed consistently poor wear resistance at all thicknesses. The IB 2.5 nm coating does provide reasonable wear protection at low loads.

Wear depths as a function of normal load for MP, BaFe and ME tapes along the parallel direction are plotted in Fig. 22.37 [47]. For the ME tape, there is negligible wear until the normal load of about 50 μN, above this load the magnetic coating fails rapidly. This observation is consistent with the scratch data. Wear depths as a function of number of cycles for MP, BaFe, and ME tapes are shown in Fig. 22.38. For the MP and BaFe particulate tapes, wear rates appear to be independent of the particulate density. Again as observed in the scratch testing, wear rate of BaFe tapes is higher than that for MP tapes. ME tapes are much more wear resistant than the particulate tapes. However, the failure of ME tapes are catastrophic as observed in scratch testing. Wear studies were performed along and across the longitudinal tape direction in high and low hardness regions. At the high hardness regions of the ME tapes, failure occurs at lower loads. Directionality effect again may arise from the columnar structure of the ME films [3, 60]. Wear profiles at various cycles at a normal load of 2 μN for MP and at 20 μN for ME tapes are shown in Fig. 22.39. For the particulate tapes, we note that polymer gets removed before the particulates do (Fig. 22.39a). Based on the wear profiles of the ME tape shown in Fig. 22.39a, we note that most wear occurs between 50 and 60 cycles which shows the catastrophic removal of the coating. It was also observed that wear debris generated during wear

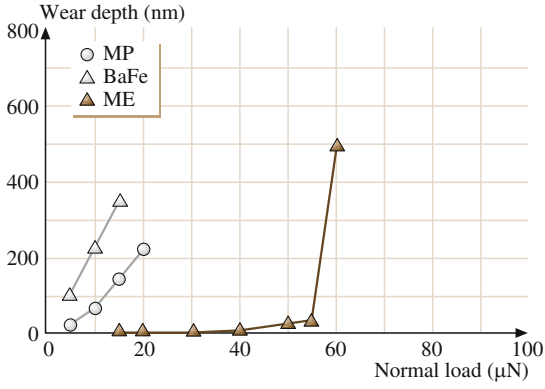

Fig. 22.37 Wear depth as a function of normal load for three tapes in the parallel direction after one cycle [47]

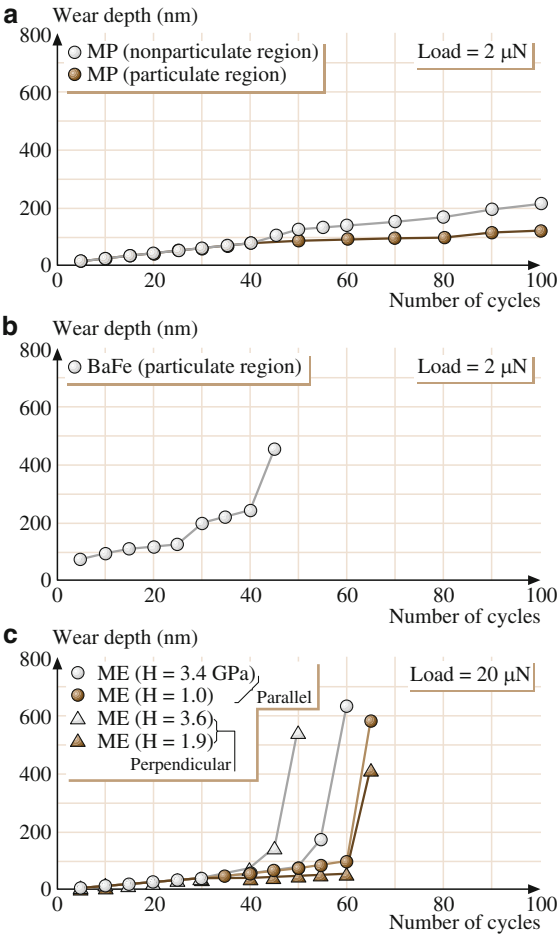

Fig. 22.38 Wear depth as a function of number of cycles for (**a**) MP, (**b**) BaFe, and (**c**) ME tapes in different regions at normal loads indicated in the figure. Note a higher load used for the ME tape in (**c**) [47]

test in all cases is loose and can easily be removed away from the scan area at light loads ($\approx$ 0.3 μN).

The average wear depth as a function of load for a PET film is shown in Fig. 22.40. Again, the wear depth increases linearly with load. Figure 22.41 shows the average wear depth as a function of number of cycles. The observed wear rate is approximately constant. PET tape substrate consists of particles sticking out on its surface to facilitate winding. Figure 22.42 shows the wear profiles as a function of number of cycles at 1 μN load on the PET film in the nonparticulate and particulate regions [45]. We note that polymeric materials tear in microwear tests. The particles do not wear readily at 1 μN. Polymer around the particles is removed but the particles remain intact. Wear in the particulate region is much smaller than that in the polymer region. We will see later that nanohardness of the particulate region is about 1.4 GPa compared to 0.3 GPa in the nonparticulate region (Table 22.3).

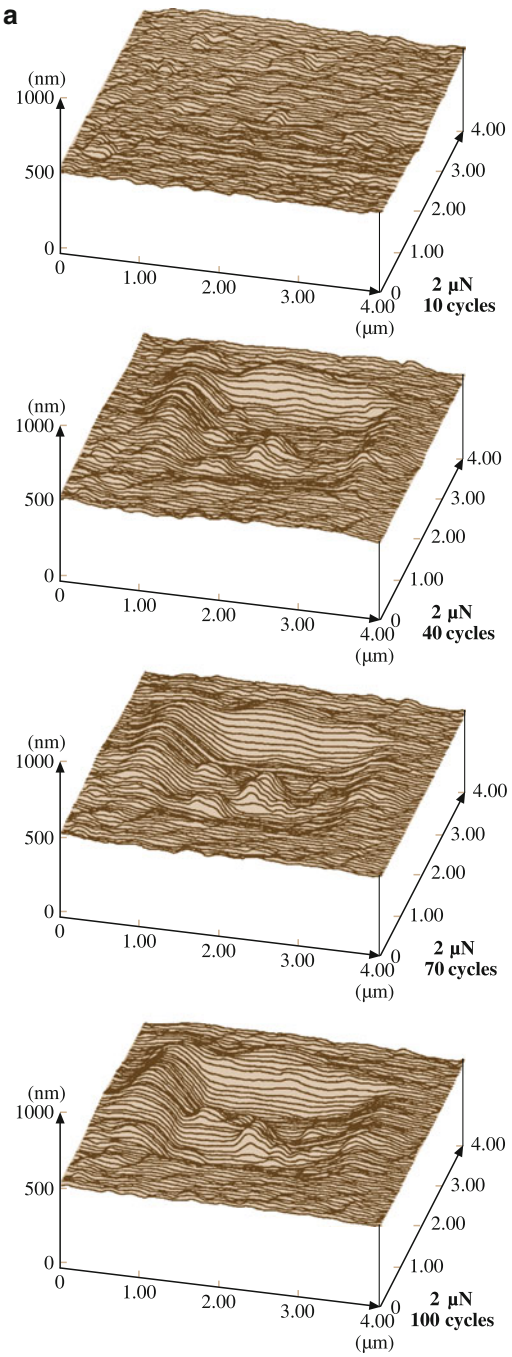

Fig. 22.39 (continued)

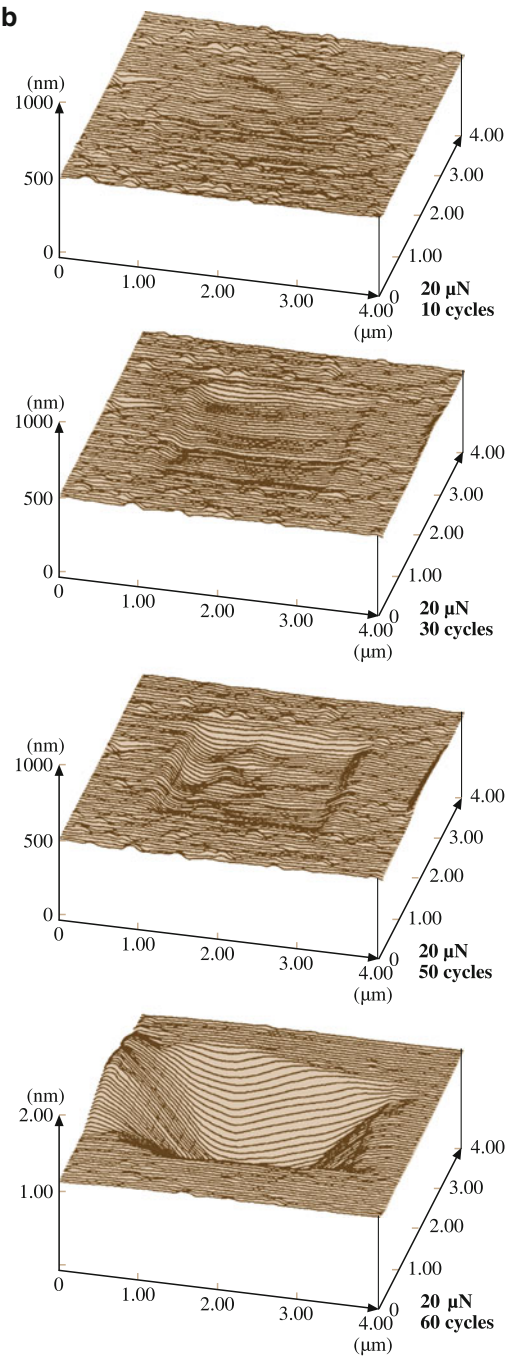

Fig. 22.39 Surface maps showing the worn region (center 2 μm × 2 μm) after various cycles of wear at (**a**) 2 μN for MP (particulate region) and at (**b**) 20 μN for ME (H = 3.4 GPa, parallel direction) tapes. Note a different *vertical scale* for the bottom profile of (**b**) [47]

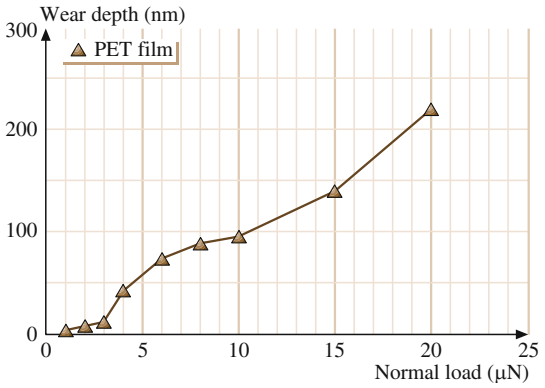

Fig. 22.40 Wear depth as a function of normal load (after one cycle) for a PET film [45]

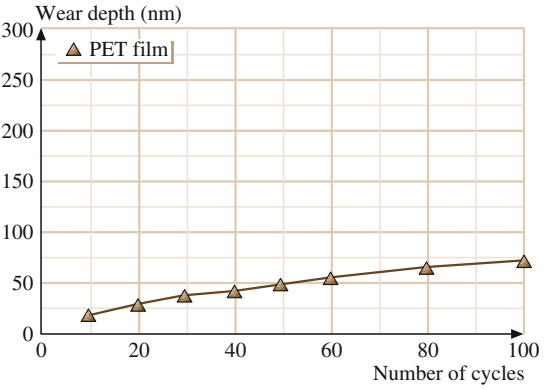

Fig. 22.41 Wear depth as a function of number of cycles at 1 μN for a PET film [45]

22.6 Indentation

22.6.1 Picoscale Indentation

Bhushan and Ruan [15] measured indentability of magnetic tapes at increasing loads on a picoscale, Fig. 22.43. In this figure, the vertical axis represents the cantilever tip deflection and the horizontal axis represents the vertical position (Z) of the sample. The "extending" and "retracting" curves correspond to the sample being moved toward or away from the cantilever tip, respectively. In this experiment, as the sample surface approaches the AFM tip fraction of a nm away from the sample (point A), the cantilever bends toward the sample (part B) because of attractive forces between the tip and sample. As we continue the forward position of the sample, it pushes the cantilever back through its original rest position (point of zero applied load) entering the repulsive region (or loading portion) of the force curve. As the sample is retracted, the cantilever deflection decreases. At point D in

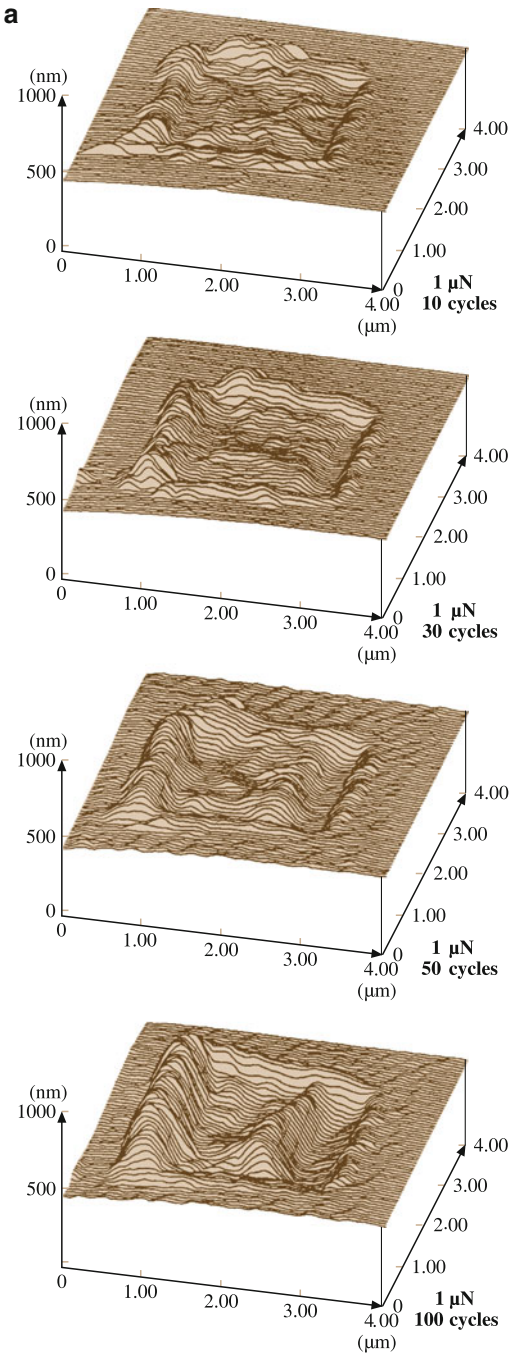

Fig. 22.42 (continued)

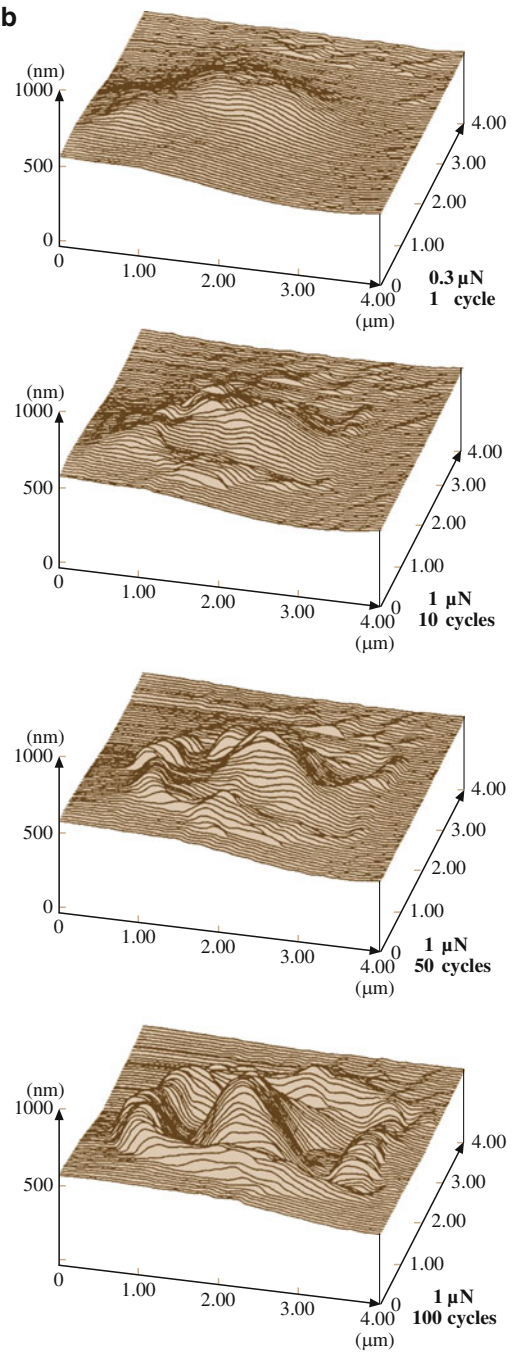

Fig. 22.42 Surface maps showing the worn region (center 2 μm × 2 μm) at 1 μN for a PET film (**a**) in the polymer region, (**b**) in the particulate region. The number of cycles are indicated in the figure [45]

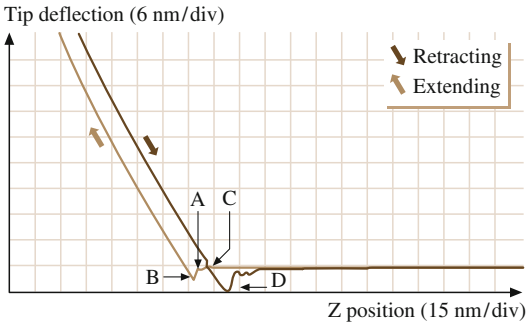

Fig. 22.43 Tip deflection (normal force) as a function of Z (separation distance) curve for a metal-particle (MP) tape. The spring constant of the cantilever used was 0.4 N/m [15]

the retracting curve, the sample is disengaged from the tip. Before the disengagement, the tip is pulled toward the sample after the zero deflection point of the force curve (point C) because of attractive forces (van der Waals forces and longer range meniscus forces). A thin layer of liquid, such as liquid lubricant and condensations of water vapor from ambient, will give rise to capillary forces that act to draw the tip towards sample at small separations. The horizontal shift between the loading and unloading curves results from the hysteresis in the PZT tube.

The left portion of the curve shows the tip deflection as a function of the sample traveling distance during sample–tip contact, which would be equal to each other for a rigid sample. However, if the tip indents into the sample, the tip deflection would be less than the sample traveling distance, or in other words, the slope of the line would be less than 1. In Fig. 22.43, we note that line in the left portion of the figure is curved with a slope of less than 1 shortly after the sample touches the tip, which suggests that the tip has indented the sample. Later, the slope is equal to 1 suggesting that the tip no longer indents the sample. This observation indicates that the tape surface is soft locally (polymer rich) but it is hard (as a result of magnetic particles) underneath. Since the curves in extending and retracting modes are identical, the indentation is elastic up to at a maximum load of about 22 nN used in the measurements.

According to Bhushan and Ruan [15], during indentation of rigid disks, the slope of the deflection curves remained constant as the disks touch and continue to push the AFM tip. The disks were not indented.

22.6.2 Nanoscale Indentation

Indentation hardness with a penetration depth as low as 5 nm can be measured using AFM. Bhushan and Koinkar [17] measured hardness of thin-film disks at load of 80, 100, and 140 μN. Hardness values were 20 GPa (10 nm), 21 GPa (15 nm) and 9 GPA (40 nm); the depths of indentation are shown in the parenthesis. The hardness value at 100 μN is much higher than at 140 μN. This is expected since the indentation depth is only about 15 nm at 100 μN which is smaller than the thickness

of carbon coating (≈ 30 nm). The hardness value at lower loads is primarily the value of the carbon coating. The hardness value at higher loads is primarily the value of the magnetic film, which is softer than the carbon coating [2]. This result is consistent with the scratch and wear data discussed previously.

For the case of hardness measurements made on magnetic thin film rigid disk at low loads, the indentation depth is on the same order at the variation in the surface roughness. For accurate measurements of indentation size and depth, it is desirable to subtract the original (unindented) profile from the indented profile. Bhushan et al. [18] developed an algorithm for this purpose. Because of hysteresis, a translational shift in the sample plane occurs during the scanning period, resulting in a shift between images captured before and after indentation. Therefore, the image for perfect overlap needs to be shifted before subtraction can be performed. To accomplish this objective, a small region on the original image was selected and the corresponding region on the indented image was found by maximizing the correlation between the two regions. (Profiles were plane-fitted before subtraction.) Once two regions were identified, overlapped areas between the two images were determined and the original image was shifted with the required translational shift and this subtracted from the indented image. An example of profiles before and after subtraction is shown in Fig. 22.44. It is easier to measure the indent on the subtracted image. At a normal load of 140 mN the hardness value of an unlubricated, as-polish

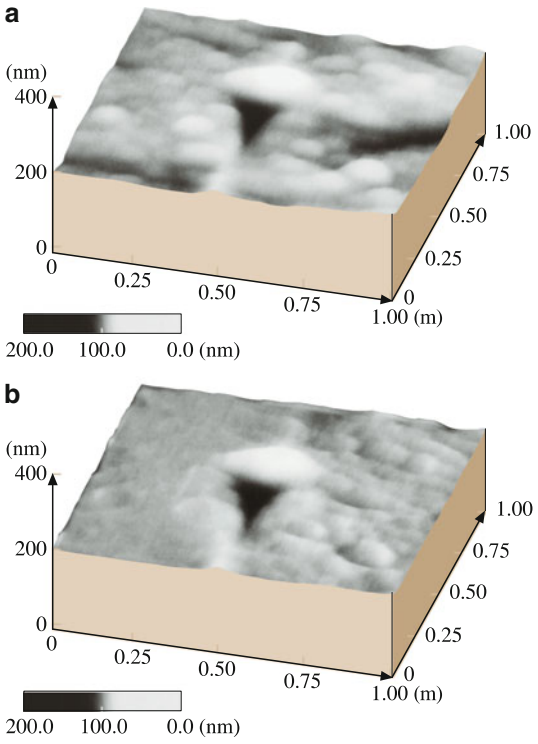

Fig. 22.44 Images with nanoindentation marks generated on a polished, unlubricated thin-film rigid disk at 140 μN (**a**) before subtraction, and (**b**) after subtraction [18]

magnetic thin film rigid disk (rms roughness = 3.3 nm) is 9.0 GPa and indentation depth is 40 nm.

For accurate measurement of nanohardness at very shallow indentation depths, depth-sensing capacitance transducer system in an AFM is used [19]. Figure 22.45a shows the hardness as a function of residual depth for three types of 100 nm thick amorphous carbon coatings deposited on silicon by sputtering, ion beam and cathodic arc processes [50]. Data on uncoated silicon are also included for comparisons. The cathodic arc carbon coating exhibits highest hardness of about 24.9 GPa, whereas the sputtered and ion beam carbon coatings exhibit hardness values of 17.2 and 15.2 GPa respectively. The hardness of Si(100) is 13.2 GPa. High hardness of cathodic arc carbon coating explains its high wear resistance, reported earlier. Figure 22.45b shows the elastic modulus as a function of residual depth for various samples. The cathodic arc coating exhibits the highest elastic modulus. Its elastic modulus decreases with an increasing residual depth, while the elastic moduli for the other carbon coatings remain almost constant. In general, hardness and elastic modulus of coatings are strongly influenced by their crystalline structure, stoichiometry and growth characteristics which depend on the deposition parameters. Mechanical properties of carbon coatings have been known to change over a wide range with sp^3–sp^2 bonding ratio and amount of hydrogen. Hydrogen is believed to play an important role in the bonding

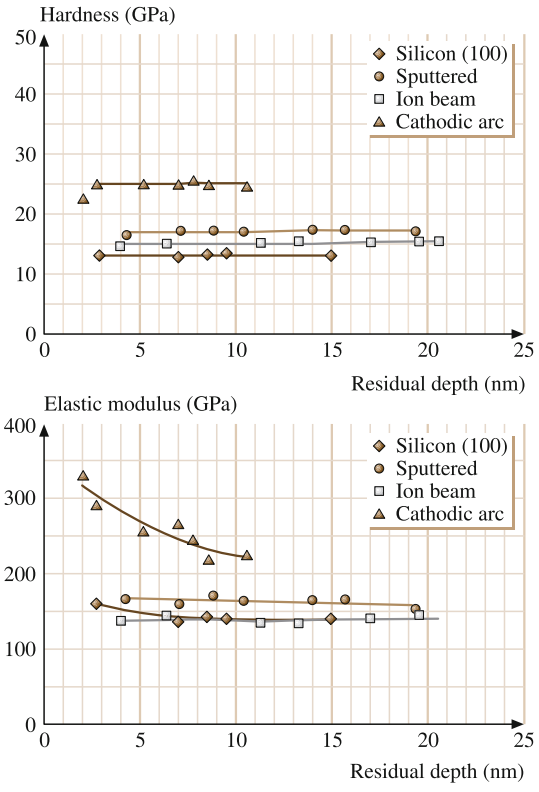

Fig. 22.45 Nanohardness and elastic modulus as a function of residual indentation depth for Si(100) and 100 nm thick coatings deposited by sputtering, ion beam and cathodic arc processes [50]

configuration of carbon atoms by helping to stabilize tetrahedral coordination of carbon atoms. Detailed mechanical characterization of amorphous carbon coatings is presented by Li and Bhushan [51, 52] and Bhushan [59].

22.6.3 Localized Surface Elasticity

By using an AFM in a so-called force modulation mode, it is possible to quantitatively measure the elasticity of soft and compliant materials with penetration depths of less than 100 nm [21, 22]. This technique has been successfully used to get localized elasticity maps of particulate magnetic tapes. Elasticity map of a tape can be used to identify relative distribution of hard magnetic/nonmagnetic ceramic particles and the polymeric binder on the tape surface which has an effect on friction and stiction at the head–tape interface. Figure 22.46 shows surface height and elasticity maps on an MP tape. The elasticity image reveals sharp variations in surface elasticity due to the composite nature of the film. As can be clearly seen, regions of high elasticity do not always correspond to high or low topography. Based on a Hertzian elastic-contact analysis, the static indentation depth of these sample during the force modulation scan is estimated to be about 1 nm. The contrast seen is influenced most strongly by material properties in the top few nanometers, independent of the composite structure beneath the surface layer. The trend in number of stiff regions has been correlated to reduced stiction problems in tapes [62].

Figure 22.47 shows the surface topography and phase image of an alumina particle embedded in the MP tape using a so-called TR mode [25, 26]. The cross-section view of the particle obtained from the topographic image is shown at the bottom as a visual aid. The edges of the particle show up darker in the TR phase angle image, which suggests that it is less viscoelastic compared to the background. The magnetic particles on top of the alumina particle are clearly visible in the TR phase image. These have

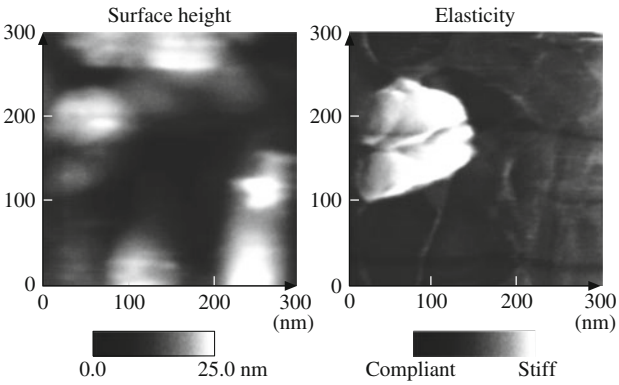

Fig. 22.46 Surface height and elasticity maps for a metal-particle tape A ($\sigma = 6.72$ nm and P–$V = 31.7$ nm). σ and P–V refer to standard deviation of surface heights and peak-to-valley distance, respectively. The *grayscale* on the elasticity map is arbitrary [21]

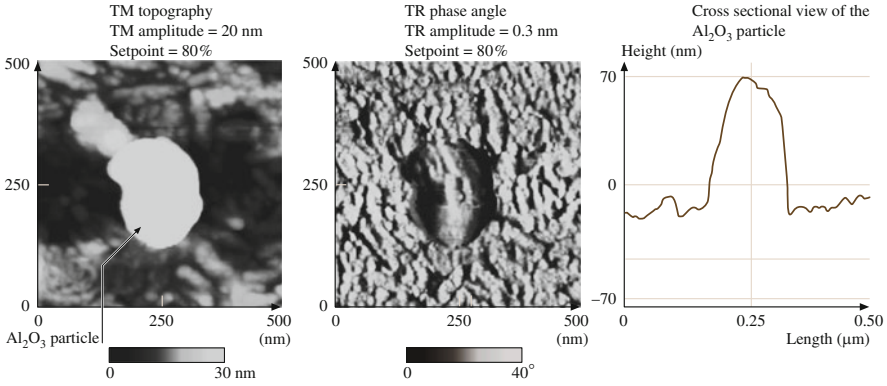

Fig. 22.47 Tapping mode (TM) topography and TR phase angle image of an alumina particle that is used as a head cleaning agent for MP tape. A cross-sectional view of the particle is also shown [25]

a brighter contrast, which is the same as that of the background. Phase contrast mapping appears to provide better resolution than stiffness mapping for magnetic tapes.

22.7 Lubrication

The boundary films are formed by physical adsorption, chemical adsorption, and chemical reaction. The physisorbed film can be either monomolecular or polymolecular thick. The chemisorbed films are monomolecular, but stoichiometric films formed by chemical reaction can have a large film thickness. In general, the stability and durability of surface films decrease in the following order: chemical reaction films, chemisorbed films and physisorbed films. A good boundary lubricant should have a high degree of interaction between its molecules and the sliding surface. As a general rule, liquids are good lubricants when they are polar and thus able to grip solid surfaces (or be adsorbed). Polar lubricants contain reactive functional groups with low ionization potential or groups having high polarizability [5]. Boundary lubrication properties of lubricants are also dependent upon the molecular conformation and lubricant spreading [63–66].

Mechanical interactions between the magnetic head and the medium in magnetic storage devices are minimized by the lubrication of the magnetic medium [2, 3]. The primary function of the lubricant is to reduce the wear of the medium and to ensure that friction remains low throughout the operation of the drive. The main challenge, though, in selecting the best candidate for a specific surface is to find a material that provides an acceptable wear protection for the entire life of the product, which can be several years in duration. There are many requirements that a lubricant must satisfy in order to guarantee an acceptable life performance. An optimum lubricant thickness is one of these requirements. If the lubricant film is too thick, excessive stiction and mechanical failure of the head-disk is observed. On the other hand, if the film is too thin, protection of the interface is compromised, and

high friction and excessive wear will result in catastrophic failure. An acceptable lubricant must exhibit properties such as chemical inertness, low volatility, high thermal, oxidative and hydrolytic stability, shear stability, and good affinity to the magnetic medium surface.

Fatty acid esters are excellent boundary lubricants, and esters such as tridecyl stearate, butyl stearate, butyl palmitate, buryl myristate, stearic acid, and myrstic acid are commonly used as internal lubricants, roughly 1–7% by weight of the magnetic coating in particulate flexible media (tapes and particulate flexible disks) [2, 3]. The fatty acids involved include those with acid groups with an even number of carbon atoms between C_{12} and C_{22}, with alcohols ranging from C_3 to C_{13}. These acids are all solids with melting points above the normal surface operating temperature of the magnetic media. This suggests that the decomposition products of the ester via lubrication chemistry during a head-flexible medium contact may be the key to lubrication.

Topical lubrication is used to reduce the wear of rigid disks and thin-film tapes [67]. Perfluoropolyethers (PFPEs) are chemically the most stable lubricants with some boundary lubrication capability, and are most commonly used for topical lubrication of rigid disks. PFPEs commonly used include Fomblin Z lubricants, made by Solvay Solexis, Inc., Milan, Italy; and Demnum S, made by Diakin, Japan; and their difunctional derivatives containing various reactive end groups, e.g., hydroxyl or alcohol (Fomblin Z-DOL and Z-TETROL), piperonyl (Fomblin AM 2001), isocyanate (Fomblin Z-DISOC), and ester (Demnum SP). Fomblin Y and Krytox 143 AD (made by Dupont USA) have been used in the past for particulate rigid disks. The difunctional derivatives are referred to as reactive (polar) PFPE lubricants. The chemical structures, molecular weights, and viscosities of various types of PFPE lubricants are given in Table 22.4. We note that rheological properties of thin-films of lubricants are expected to be different from their bulk properties. Fomblin Z and Demnum S are linear PFPE, and Fomblin Y and Krytox 143AD are branched PFPE, where the regularity of the chain is perturbed by $–CF_3$ side groups. The bulk viscosity of Fomblin Y and Krytox 143 AD is almost an order of magnitude higher than the Z type. Fomblin Z is thermally decomposed more rapidly than Y [5]. The molecular diameter is about 0.8 nm for these lubricant molecules. The monolayer thickness of these molecules depends on the molecular conformations of the polymer chain on the surface [64, 65].

The adsorption of the lubricant molecules on a magnetic disk surface is due to van der Waals forces, which are too weak to offset the spin-off losses, or to arrest displacement of the lubricant by water or other ambient contaminants. Considering that these lubricating films are on the order of a monolayer thick and are required to function satisfactorily for the duration of several years, the task of developing a workable interface is quite formidable. An approach aiming at alleviating these shortcomings is to enhance the attachment of the molecules to the overcoat, which, for most cases, is sputtered carbon. There are basically two approaches which have been shown to be successful in bonding the monolayer to the carbon. The first relies on exposure of the disk lubricated with neutral PFPE to various forms of radiation, such as low-energy X-ray [68], nitrogen plasma [69], or far ultraviolet

Table 22.4 Chemical structure, molecular weight, and viscosity of perfluoropolyether lubricants

Lubricant	Formula	Molecular weight (Dalton)	Kinematic viscosity cSt(mm^2/s)
Fomblin Z-25	$CF_3–O–(CF_2–CF_2–O)_m–(CF_2–O)_n–CF_3$	12,800	250
Fomblin Z-15	$CF_3–O–(CF_2–CF_2–O)_m–(CF_2–O)_n–CF_3$ $(m/n \approx 2/3)$	9,100	150
Fomblin Z-03	$CF_3–O–(CF_2–CF_2–O)_m–(CF_2–O)_n–CF_3$	3,600	30
Fomblin Z-DOL	$HO–CH_2–CF_2–O–(CF_2–CF_2–O)_m–(CF_2–O)_n–CF_2–CH_2–OH$	2,000	80
Fomblin AM2001	Piperonyl–$O–CH_2–CF_2–O–(CF_2–CF_2–O)_m–(CF_2–O)_n–CF_2–O$–piperonyl[a]	2,300	80
Fomblin Z-DISOC	$O–CN–C_6H_3–(CH_3)–NH–CO–CF_2–O–(CF_2–CF_2–O)_n–(CF_2–O)_m–CF_2–CO–NH–C_6H_3–(CH_3)–N–CO$	1,500	160
Fomblin YR	$CF_3–O–(C(F)(CF_3)–CF_2–O)_m(CF_2–O)_n–CF_3$ $(m/n \approx 40/1)$	6,800	1,600
Demnum S-100	$CF_3–CF_2–CF_2–O–(CF_2–CF_2–CF_2–O)_m–CF_2–CF_3$	5,600	250
Krytox 143 AD	$CF_3–CF_2–CF_2–O–(C(F)(CF_3)–CF_2–O)_m–CF_2–CF_3$	2,600	–

[a]3,4-methylenedioxybenzyl

(e.g., 185 nm) [70]. Another approach is to use chemically active PFPE molecules, where the various functional (reactive) end groups offer the opportunity of strong attachments to specific interface. These functional groups can react with surfaces and bond the lubricant to the disk surface, which reduces its loss due to spin off and evaporation. Bonding of lubricant to the disk surface depends upon the surface cleanliness. After lubrication, the disk is generally heated at 150°C for 30 min to 1 h to improve the bonding. If only a bonded lubrication is desired, the unbonded fraction can be removed by washing it off for 60 s with a non-Freon solvent (FC-72). Their main advantage is their ability to enhance durability without the problem of stiction usually associated with weakly bonded lubricants [2].

Boundary Lubrication Studies

Koinkar and Bhushan [29] and Liu and Bhushan [30] studied friction, adhesion, and durability of Z-15 and Z-DOL (bonded and washed, BW) lubricants on Si(100) surface. To investigate the friction properties of Si(100), Z-15, and Z-DOL(BW),

the friction force versus normal load curves were obtained by making friction measurements at increasing normal loads, Fig. 22.48. An approximately linear response of all three samples is observed in the load range of 5–130 nN. From the horizontal intercept at zero value of friction force, adhesive force can be obtained. The adhesive forces for three samples were also measured using the force calibration plot technique. The adhesive force data obtained by the two techniques are summarized in Fig. 22.49, and the trends in the data obtained by two techniques are similar. The friction force and adhesive force of solid-like Z-DOL(BW) are consistently smaller than that for Si(100), but these values of liquid-like Z-15 lubricant is higher than that of Si(100). The presence of mobile Z-15 lubricant film increases adhesive force as compared to that of the Si(100) by meniscus formation. Whereas, the presence of Z-DOL(BW) film reduces the adhesive force because of absence of mobile liquid. See schematics at the bottom of Fig. 22.49. It is well known that in computer rigid disk drives, the stiction force increases rapidly with an increase in rest time between head and the disk [2]. The effect of rest time of 180 s on the friction force, adhesive force, and coefficient of friction for three samples are summarized in Fig. 22.50. It is seen that time effect is present in Si(100) and Z-15 with mobile liquid present. Whereas, time effect is not present for Z-DOL (BW) because of the absence of mobile liquid.

To study lubricant depletion during microscale measurements, nanowear studies were conducted using Si_3N_4 tips. Measured friction as a function of number of cycles for Si(100) and silicon surface lubricated with Z-15 and Z-DOL (BW) lubricants are presented in Fig. 22.51. An area of 2 μm × 2 μm was scanned at a normal force of 70 nN. As observed before, friction force and coefficient of friction of Z-15 is higher than that of Si(100) with the lowest values for Z-DOL(BW). During cycling, friction force and coefficient of friction of Si(100) show a slight decrease during initial few cycles, then remain constant. This is related to the

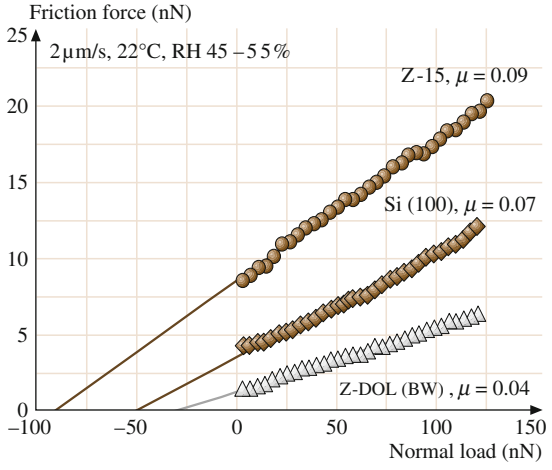

Fig. 22.48 Friction force versus normal load curves for Si(100), 2.8 nm thick Z-15 film, and 2.3 nm thick Z-DOL (BW) film at 2 μm/s, and in ambient air sliding against a Si_3N_4 tip. Based on these curves, coefficient of friction (μ) and adhesive force can be calculated [30]

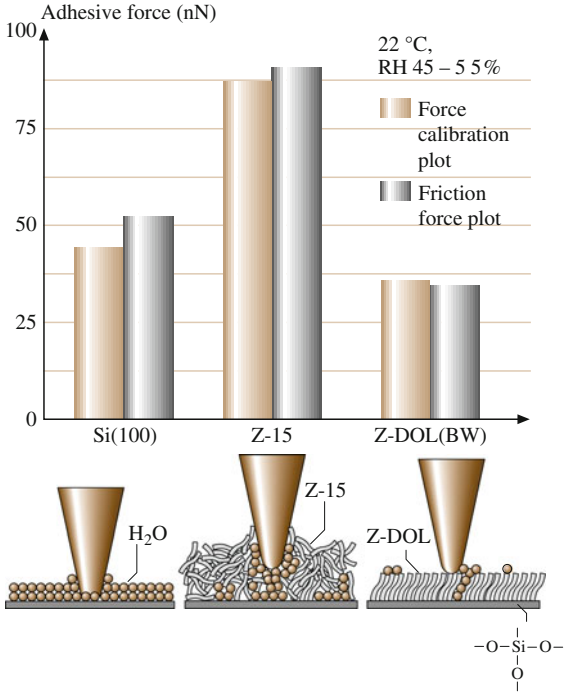

Fig. 22.49 Summary of the adhesive forces of Si(100), 2.8 nm thick Z-15 film, and 2.3 nm thick Z-DOL(BW) film. The schematic (*bottom*) shows the effect of meniscus formation between the AFM tip and the sample surface on the adhesive and friction forces [30]

removal of the top adsorbed layer. In the case of Z-15 film, the friction force and coefficient of friction show an increase during the initial few cycles and then approach to higher and stable values. This is believed to be caused by the attachment of the Z-15 molecules onto the tip. The molecular interaction between these attached molecules to the tip and molecules on the film surface is responsible for an increase in the friction. But after several scans, this molecular interaction reaches to the equilibrium and after that friction force and coefficient of friction remain constant. In the case of Z-DOL (BW) film, the friction force and coefficient of friction start out to be low and remain low during the entire test for 100 cycles. It suggests that Z-DOL (BW) molecules do not get attached or displaced as readily as Z-15.

22.8 Closure

Atomic force microscope/friction force microscope (AFM/FFM) have been successfully used for measurements of surface roughness, friction, adhesion, scratching, wear, indentation, and lubrication on a micro to nanoscales. Commonly measured

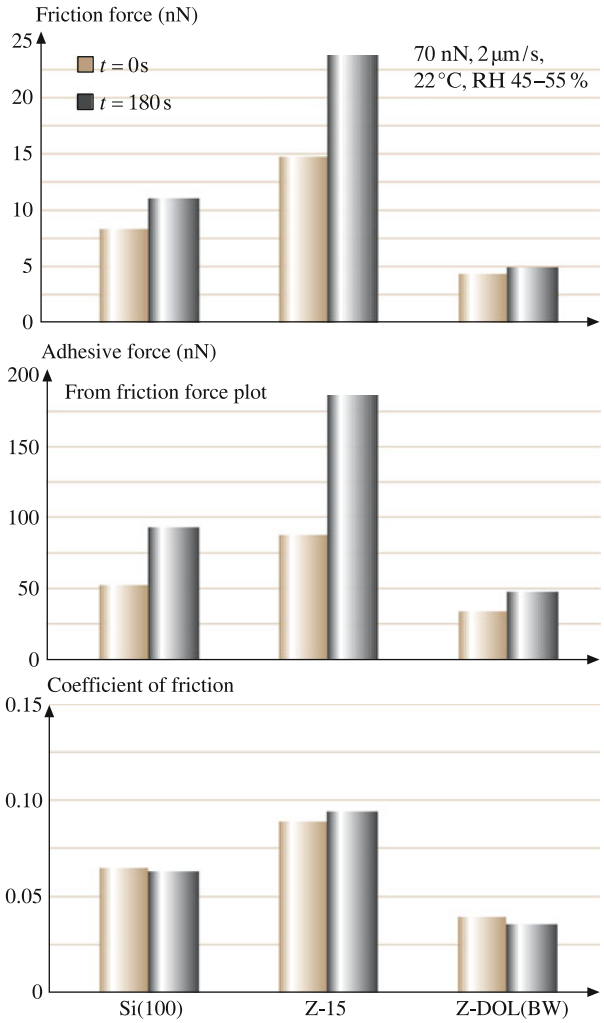

Fig. 22.50 Summary of rest time effect on friction force, adhesive force, and coefficient of friction of Si(100), 2.8 nm thick Z-15 film, and 2.3 nm thick Z-DOL(BW) film [30]

roughness parameters are scale dependent, requiring the need of scale-independent fractal parameters to characterize surface roughness. A generalized fractal analysis is presented which allows the characterization of surface roughness by two scale-independent parameters. Local variation in microscale friction force is found to correspond to the local surface slope suggesting that a ratchet mechanism is responsible for this variation. Directionality in the friction is observed on both micro- and macro-scales because of surface topography. Microscale friction is found to be significantly smaller than the macro-scale friction as there is less plowing contribution in microscale measurements.

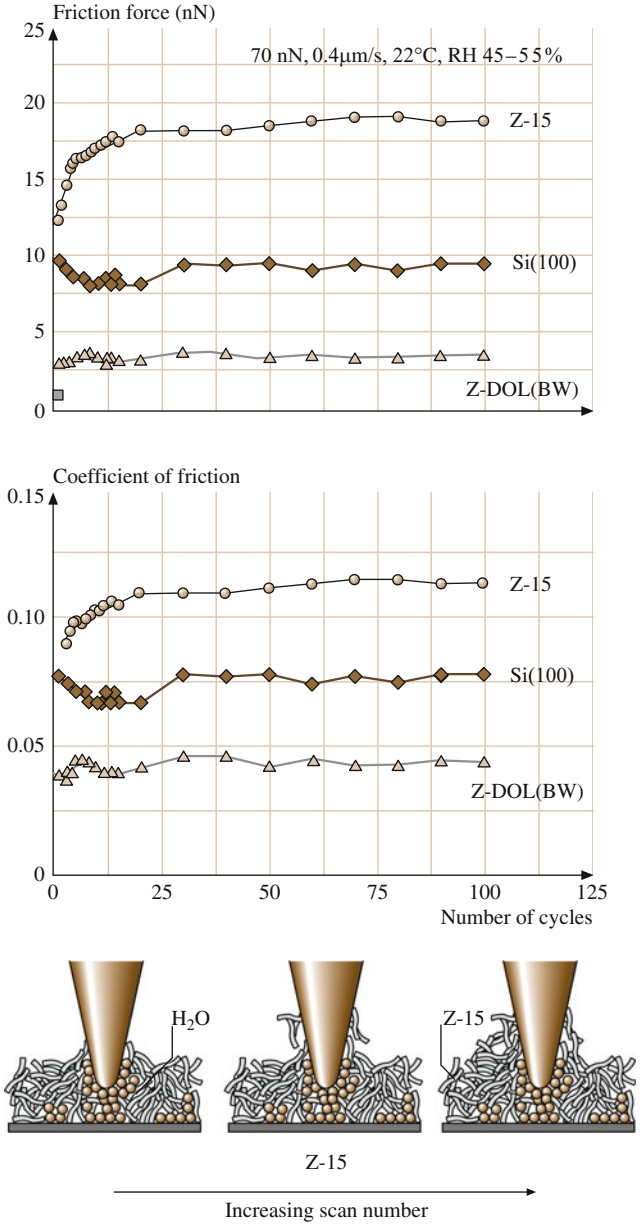

Fig. 22.51 Friction force and coefficient of friction versus number of sliding cycles for Si(100), 2.8 nm thick Z-15, and 2.3 nm thick Z-DOL (BW) film at 70 nN, 0.8 μm/s, and in ambient air. Schematic bottom shows that some liquid Z-15 molecules can be attached onto the tip. The molecular interaction between the attached molecules onto the tip with the Z-15 molecules in the film results in an increase of the friction force with multiscanning [30]

Wear rates for particulate magnetic tapes and polyester tape substrates are approximately constant for various loads and test durations. However, for magnetic disks and magnetic tapes with a multilayered thin-film structure, the wear of the diamondlike amorphous carbon overcoat in the case of disks and magnetic layer in the case of tapes, is catastrophic. Breakdown of thin-films can be detected with AFM. Evolution of the wear has also been studied using AFM. We find that the wear is initiated at nanoscratches. Amorphous carbon films as thin as 3.5 nm are deposited as continuous films and exhibit some wear life. Wear life increases with an increase in film thickness. Carbon coatings deposited by cathodic arc and ECR-CVD processes are superior in wear and mechanical properties followed by ion beam and sputtering processes. AFM has been modified for nanoindentation hardness measurements with depth of indentation as low as 5 nm. Scratching and indentation on nanoscales are the powerful ways of evaluation of the mechanical integrity of ultrathin films.

AFM/FFM friction experiments show that lubricants with polar (reactive) end groups dramatically increase the load or contact pressure that a liquid film can support before solid–solid contact and thus exhibit long durability. The lubricants with the absence of mobile liquid exhibit low friction and adhesion and don't exhibit rest time effect.

References

1. B. Bhushan, *Tribology of Magnetic Storage Systems*, vol. 3 (CRC Press, Boca Raton, 1994), pp. 325–374
2. B. Bhushan, *Tribology and Mechanics of Magnetic Storage Devices*, 2nd edn. (Springer, Berlin, 1996)
3. B. Bhushan, *Mechanics and Reliability of Flexible Magnetic Media*, 2nd edn. (Springer, Berlin, 2000)
4. B. Bhushan, *Macro- and Microtribology of Magnetic Storage Devices*. Materials, Coatings, and Industrial Applications, vol. 2 (CRC Press, Boca Raton, 2001), pp. 1413–1513
5. B. Bhushan, *Magnetic Recording Surfaces* (Butterworth-Heinemann, Boston, 1993), pp. 116–133
6. B. Bhushan, *Nanotribology and its Applications to Magnetic Storage Devices and MEMS* (Kluwer, Dordrecht, 1995), pp. 367–395
7. B. Bhushan, Micro/nanotribology and its application to magnetic storage devices and mems. Tribol. Int. **28**, 85–95 (1995)
8. B. Bhushan, J.N. Israelachvili, U. Landman, Nanotribology: Friction, wear and lubrication at the atomic scale. Nature **374**, 607–616 (1995)
9. B. Bhushan, *Micro/Nanotribology and its Applications*. NATO ASI Ser. 330 (Kluwer, Dordrecht,1997)
10. B. Bhushan, *Handbook of Micro/Nanotribology*, 2nd edn. (CRC Press, Boca Raton, 1999)
11. B. Bhushan, *Fundamentals of Tribology and Bridging the Gap Between the Macro- and Micro/Nanoscales*. NATO Sci. Ser. II (Kluwer, Dordrecht, 1997)
12. B. Bhushan, *Introduction to Tribology* (Wiley, New York, 2002)
13. B. Bhushan (ed.), *Springer Handbook of Nanotechnology* (Springer, Berlin, 2004)

14. J. Ruan, B. Bhushan, Atomic-scale friction measurements using friction force microscopy: Part i – General principles and new measurement techniques. ASME J. Tribol. **116**, 378–388 (1994)
15. B. Bhushan, J. Ruan, Atomic-scale friction measurements using friction force microscopy: Part ii – Application to magnetic media. ASME J. Tribol. **116**, 389–396 (1994)
16. B. Bhushan, V.N. Koinkar, Tribological studies of silicon for magnetic recording applications. J. Appl. Phys. **75**, 5741–5746 (1994)
17. B. Bhushan, V.N. Koinkar, Nanoindentation hardness measurements using atomic force microscopy. Appl. Phys. Lett. **64**, 1653–1655 (1994)
18. B. Bhushan, V.N. Koinkar, J. Ruan, Microtribology of magnetic media. Proc. Inst. Mech. Eng. Part J, Eng. Tribol. **208**, 17–29 (1994)
19. B. Bhushan, A.V. Kulkarni, W. Bonin, J.T. Wyrobek, Nanoindentation and picoindentation measurements using a capacitance transducer system in atomic force microscopy. Philos. Mag. **74**, 1117–1128 (1996)
20. S. Sundararajan, B. Bhushan, Development of a continuous microscratch technique in an atomic force microscopy and its applications to study scratch resistance of ultra-thin hard amorphous carbon coatings. J. Mater. Res. **16**, 437–445 (2001)
21. D. DeVecchio, B. Bhushan, Localized surface elasticity measurements using an atomic force microscope. Rev. Sci. Instrum. **68**, 4498–4505 (1997)
22. V. Scherer, B. Bhushan, U. Rabe, W. Arnold, Local elasticity and lubrication measurements using atomic force and friction force microscopy at ultrasonic frequencies. IEEE Trans. Mag. **33**, 4077–4079 (1997)
23. W.W. Scott, B. Bhushan, Use of phase imaging in atomic force microscopy for measurement of viscoelastic contrast in polymer nanocomposites and molecularly-thick lubricant films. Ultramicroscopy **97**, 151–169 (2003)
24. B. Bhushan, J. Qi, Phase contrast imaging of nanocomposites and molecularly-thick lubricant films in magnetic media. Nanotechnology **14**, 886–895 (2003)
25. T. Kasai, B. Bhushan, L. Huang, C. Su, Topography and phase imaging using the torsional resonance mode. Nanotechnology **15**, 731–742 (2004)
26. B. Bhushan, T. Kasai, A surface topography-independent friction measurement technique using torsional resonance mode in an afm. Nanotechnology **15**, 923–935 (2004)
27. B. Bhushan, T. Miyamoto, V.N. Koinkar, Microscopic friction between a sharp diamond tip and thin-film magnetic rigid disks by friction force microscopy. Adv. Info. Storage Syst. **6**, 151–161 (1995)
28. V.N. Koinkar, B. Bhushan, Microtribological studies of Al_2O_3, Al_2O_3–TiC, polycrystalline and single-crystal Mn–Zn ferrite and SiC head slider materials. Wear **202**, 110–122 (1996)
29. V.N. Koinkar, B. Bhushan, Microtribological studies of unlubricated and lubricated surfaces using atomic force/friction force microscopy. J. Vac. Sci. Technol. A **14**, 2378–2391 (1996)
30. H. Liu, B. Bhushan, Nanotribological characterization of molecularly-thick lubricant films for applications to mems/nems by afm. Ultramicroscopy **97**, 321–340 (2003)
31. B. Bhushan, Magnetic slider/rigid disk substrate materials and disk texturing techniques – status and future outlook. Adv. Info. Storage Syst. **5**, 175–209 (1993)
32. B. Bhushan, M. Dominiak, J.P. Lazzari, Contact- start-stop studies with silicon planar head sliders against thin-film disks. IEEE Trans. Mag. **28**, 2874–2876 (1992)
33. B. Bhushan, G.S. Blackman, Atomic force microscopy of magnetic rigid disks and sliders and its applications to tribology. ASME J. Tribol. **113**, 452–458 (1991)
34. P.I. Oden, A. Majumdar, B. Bhushan, A. Padmanabhan, J.J. Graham, Afm imaging, roughness analysis and contact mechanics of magnetic tape and head surfaces. ASME J. Tribol. **114**, 666–674 (1992)
35. S. Ganti, B. Bhushan, Generalized fractal analysis and its applications to engineering surfaces. Wear **180**, 17–34 (1995)
36. C.Y. Poon, B. Bhushan, Comparison of surface roughness measurements by stylus profiler, afm and non-contact optical profiler. Wear **190**, 76–88 (1995)

37. C.Y. Poon, B. Bhushan, Surface roughness analysis of glass–ceramic substrates and finished magnetic disks, and Ni–P coated Al–Mg and glass substrates. Wear **190**, 89–109 (1995)
38. V.N. Koinkar, B. Bhushan, Effect of scan size and surface roughness on microscale friction measurements. J. Appl. Phys. **81**, 2472–2479 (1997)
39. A. Majumdar, B. Bhushan, Role of fractal geometry in roughness characterization and contact mechanics of surfaces. ASME J. Tribol. **112**, 205–216 (1990)
40. A. Majumdar, B. Bhushan, Fractal model of elastic-plastic contact between rough surfaces. ASME J. Tribol. **113**, 1–11 (1991)
41. B. Bhushan, A. Majumdar, Elastic-plastic contact model for bifractal surfaces. Wear **153**, 53–64 (1992)
42. B. Bhushan, Contact mechanics of rough surfaces in tribology: Single asperity contact. Appl. Mech. Rev. **49**, 275–298 (1996)
43. B. Bhushan, Contact mechanics of rough surfaces in tribology: Multiple asperity contact. Tribol. Lett. **4**, 1–35 (1998)
44. B. Bhushan, W. Peng, Contact mechanics of multilayered rough surfaces. Appl. Mech. Rev. **55**, 435–480 (2002)
45. B. Bhushan, V.N. Koinkar, Microtribology of pet polymeric films. Tribol. Trans. **38**, 119–127 (1995)
46. B. Bhushan, V.N. Koinkar, Macro and microtribological studies of CrO_2 video tapes. Wear **180**, 9–16 (1995)
47. B. Bhushan, V.N. Koinkar, Microtribology of metal particle, barium ferrite and metal evaporated magnetic tapes. Wear **181–183**, 360–370 (1995)
48. B. Bhushan, V.N. Koinkar, Microscale mechanical and tribological characterization of hard amorphous carbon coatings as thin as 5 nm for magnetic disks. Surf. Coat. Technol. **76–77**, 655–669 (1995)
49. V.N. Koinkar, B. Bhushan, Microtribological properties of hard amorphous carbon protective coatings for thin-film magnetic disks and heads. Proc. Inst. Mech. Eng. Part J. Eng. Tribol. **211**, 365–372 (1997)
50. A.V. Kulkarni, B. Bhushan, Nanoindentation measurements of amorphous carbon coatings. J. Mater. Res. **12**, 2707–2714 (1997)
51. X. Li, B. Bhushan, Micro/nanomechanical and tribological characterization of ultra-thin amorphous carbon coatings. J. Mater. Res. **14**, 2328–2337 (1999)
52. X. Li, B. Bhushan, Mechanical and tribological studies of ultra-thin hard carbon overcoats for magnetic recording heads. Z. Metallkd. **90**, 820–830 (1999)
53. S. Sundararajan, B. Bhushan, Micro/nanotribology of ultra-thin hard amorphous carbon coatings using atomic force/friction force microscopy. Wear **225–229**, 678–689 (1999)
54. B. Bhushan, S. Sundararajan, Micro/nanoscale friction and wear mechanisms of thin films using atomic force and friction force microscopy. Acta Mater. **46**, 3793–3804 (1998)
55. J. Ruan, B. Bhushan, Frictional behavior of highly oriented pyrolytic graphite. J. Appl. Phys. **76**, 8117–8120 (1994)
56. S. Sundararajan, B. Bhushan, Topography-induced contributions to friction forces measured using an atomic force/friction force microscope. J. Appl. Phys. **88**, 4825–4831 (2000)
57. B. Bhushan, V.N. Koinkar, Microtribological studies of doped single-crystal silicon and polysilicon films for mems devices. Sensor Actuator A **57**, 91–102 (1997)
58. S. Sundararajan, B. Bhushan, Micro/nanotribological studies of polysilicon and SiC films for mems applications. Wear **217**, 251–261 (1998)
59. B. Bhushan, Chemical, mechanical and tribological characterization of ultra-thin and hard amorphous carbon coatings as thin as 3.5 nm: Recent developments. Diam. Relat. Mater. **8**, 1985–2015 (1999)
60. H. Hibst, *Metal Evaporated Tapes and Co–Cr Media for High Definition Video Recording* (Kluwer, Dordrecht, 1993), pp. 137–159
61. M.Y. Chu, B. Bhushan, L. DeJonghe, Wear behavior of ceramic sliders in sliding contact with rigid magnetic thin-film disks. Tribol. Trans. **35**, 603–610 (1992)

62. B. Bhushan, S. Sundararajan, W.W. Scott, S. Chilamakuri, Stiction analysis of magnetic tapes. IEEE Trans. Mag. **33**, 3211–3213 (1997)
63. V.J. Novotny, I. Hussla, J.M. Turlet, M.R. Philpott, Liquid polymer conformation on solid surfaces. J. Chem. Phys. **90**, 5861–5868 (1989)
64. V.J. Novotny, Migration of liquid polymers on solid surfaces. J. Chem. Phys. **92**, 3189–3196 (1990)
65. C.M. Mate, V.J. Novotny, Molecular conformation and disjoining pressures of polymeric liquid films. J. Chem. Phys. **94**, 8420–8427 (1991)
66. C.M. Mate, Application of disjoining and capillary pressure to liquid lubricant films in magnetic recording. J. Appl. Phys. **72**, 3084–3090 (1992)
67. B. Bhushan, Z. Zhao, Macro- and microscale studies of molecularly-thick boundary layers of perfluoropolyether lubricants for magnetic thin-film rigid disks. J. Info. Storage Proc. Syst. **1**, 1–21 (1999)
68. R. Heideman, M. Wirth, Transforming the lubricant on a magnetic disk into a solid fluorine compound. IBM Technol. Disclosure Bull. **27**, 3199–3205 (1984)
69. A.M. Homola, L.J. Lin, D.D. Saperstein. Process for bonding lubricant to a thin film magnetic recording disk (1990)
70. D.D. Saperstein, L.J. Lin, Improved surface adhesion and coverage of perfluoropolyether lubricant following far-uv irradiation. Langmuir **6**, 1522–1524 (1990)